



# A single source method to generate Ru-Ni-MgO catalysts for methane dry reforming and the kinetic effect of Ru on carbon deposition and gasification

Haibin Zhou, Tingting Zhang, Zhijun Sui, Yi-An Zhu, Chen Han, Kake Zhu\*, Xinggui Zhou

UNILAB, State Key Lab of Chemical Engineering, School of Chemical Engineering, East China University of Science and Technology, 130 Meilong Road, Shanghai 200237, PR China

## ARTICLE INFO

### Keywords:

Methane  
Carbon dioxide  
Dry reforming  
Ru  
Kinetics

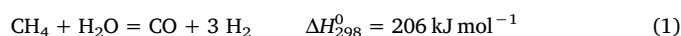
## ABSTRACT

A single precursor  $\text{Ru}_x\text{Ni}_y\text{Mg}_{1-x-y}(\text{OH})(\text{OCH}_3)$  derived from solvothermal synthesis was used to generate Ru-Ni-MgO catalysts for methane reforming with  $\text{CO}_2$ . Calcination-reduction pretreatment of precursors could easily cause segregation of Ru and formation of both large and small metallic particles as  $\text{RuO}_2$  has limited solubility in NiO-MgO solid solution. Uniform small Ru-Ni alloy particles could only be produced within their limited alloying composition range through direct reduction pretreatment of the precursor. Catalysts derived from calcination-reduction exhibited low initial activity that increased with time-on-stream, whereas catalysts derived from direct reduction demonstrated high and steady activity. Over spent catalysts, Ru was found to have changed the type of deposited carbon from a recalcitrant graphitic one that could only be gasified by  $\text{O}_2$  to a soft type that can be facily gasified by  $\text{CO}_2$ . Kinetic studies showed that Ru increased the activation barrier for the rate determining  $\text{CH}_4$  dissociation step and thereby slows down the carbon deposition rate. A first order reaction dependence for  $\text{CH}_4$  pressure variation and zeroth for  $\text{CO}_2$  pressure change for pristine Ni- and Ru-catalysts was identified, while a first order and a deviation from zeroth order for  $\text{CH}_4$  and  $\text{CO}_2$  pressure variation were observed on bimetallic Ru-Ni catalyst. Such a deviation is associated with the oxyphilic nature of Ru that is enriched in the alloy surface under reforming conditions. The effects of Ru on carbon gasification over spent catalysts were investigated using a modified  $\text{CO}_2$ -TPO measurement based on an extrapolated Wigner–Polanyi equation for carbon gasification. Ru was found to accelerate carbon gasification by increasing the pre-exponential factor for  $\text{CO}_2$  oxidation of carbon, albeit a disfavored elevated activation barrier was obtained, thus showing a strong compensation effect. Carbon gasification is favored in high concentration of  $\text{CO}_2$  and at high temperatures for Ru-Ni catalyst.

## 1. Introduction

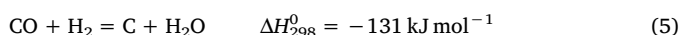
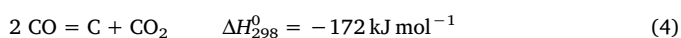
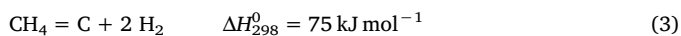
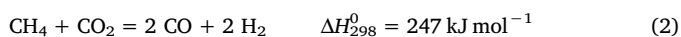
The global temperature rise concern associated with anthropogenic  $\text{CO}_2$  emissions into the Earth's atmosphere has motivated research interests towards  $\text{CO}_2$  disposal, sequestration, removal and utilization.  $\text{CH}_4$ , as the dominant component of natural gas, is commercially used mainly through methane steam reforming (SRM, reaction 1), auto-thermal reforming and partial oxidation, yielding syngas as feedstock for methanol production, Fischer-Tropsch synthesis, and so forth.  $\text{CH}_4$  reforming with  $\text{CO}_2$ , also referred to as methane dry reforming (DRM, reaction 2), has attracted growing interests recently for three advantages with respect to SRM. First, it is a potential way to consume two natural abundant greenhouse gases into a versatile chemical feedstock, and may be potentially used to convert  $\text{CO}_2$ -rich natural gas without the expensive separation processes [1]. Second, the syngas produced from DRM has a relatively low  $\text{CO}/\text{H}_2$  ratio that is more

suitable to some specific downstream use, such as the production of high alcohols and acetic acid [2]. Third, it is possible to design suitable combined  $\text{CO}_2$ - and steam-reforming process to produce syngas with adjustable compositions [1,3–5], to meet diversified downstream use. Although noble metals, such as Ru, Pt, Pd, Ir exhibit excellent carbon-resistant properties [6], Ni is preferred for large-scale industrial use owing to the wide availability and associated low cost. One major obstacle that hampers the commercialization of DRM is carbon deposition on Ni surfaces. From reaction mechanism and kinetic perspectives, SRM and DRM are alike and the strategies to circumvent carbon deposition for SRM can be extrapolated to DRM [7–9]. Nonetheless, the high carbon formation potential implied by the low C/H ratio of DRM requires more robust carbon-resistant catalyst to be advanced to meet the severe operation conditions [1,4].



\* Corresponding author.

E-mail address: [kakezhu@ecust.edu.cn](mailto:kakezhu@ecust.edu.cn) (K. Zhu).



Three reactions can potentially lead to carbon deposition on Ni surfaces, i.e., methane fragmentation (reaction 3), CO disproportionation (Boudouard reaction, reaction 4) and CO reduction by  $\text{H}_2$  (reaction 5). Under ambient pressure, thermodynamic estimation suggests that methane fragmentation occurs only at temperatures above 557 °C, whereas CO disproportionation and CO reduction by  $\text{H}_2$  take place below 700 °C and 673 °C, respectively [10]. The endothermic nature of DRM suggests that only under high operation temperatures can substantial conversions be achieved. Practically, only less than 2.5 vol.% of unreactive components can be tolerated for downstream use of syngas [4]. Consequently, DRM is operated at temperatures higher than 800 °C to satisfy high conversions, such that  $\text{CH}_4$  fragmentation becomes the only thermodynamically possible carbon deposition process. Carbon deposition occurs because the Ni surface has a strong affinity to carbon species, especially on under-coordinated surface sites such as step sites [7,11]. Deprotonation of  $\text{CH}_4$  produces atomic C\* (denoted as C $\alpha$  by some authors) on Ni surface [7], atomic C\* may form C–C bonds to afford polymeric carbon species (also known as C $\beta$ ) on Ni surface at under-coordinated sites where it binds strongly and coverage can increase accordingly [12,13]. The two carbon species can be gasified to CO under reforming conditions, henceforth, a dynamic clean surface is maintained kinetically [13]. Nevertheless, the accumulation of carbon above a certain threshold concentration will lead to the nucleation of carbon to form carbon island, encapsulating carbon, or even whisker carbon [11]. Surface diffusion of nucleated carbon from step sites to terrace sites results in the formation of whisker carbon with atop Ni particle, meanwhile, Ni particles depart away from their support [11]. The carbon deposition does not necessarily cause catalyst deactivation, for the low active surface area loss as a result of carbon diffusion [4]. However, whisker carbon has a strong mechanical strength and tends to pulverize catalyst pellets, increase pressure drop, plug reactor and eventually interrupt continuous operation [4]. Gasification of deposited carbon on Ni surface mainly takes place before their nucleation. Once whisker carbon is formed, it is difficult to gasify under reforming conditions.

In accordance with the whisker carbon formation mechanism, several strategies have been developed to suppress carbon deposition on Ni catalysts. 1. Preparing ultra-small Ni particles. Carbon islands formed on tiny Ni particles are small, unstable and tend to disappear by gasification [7], it has been also experimentally observed that small Ni particles are more robust towards carbon deposition [14–18]. For instance, reduced Ni-substituted barium hexaaluminate [19], pyrochlore [20] and Ni-MgO solid solution [15,16] catalysts possess tiny Ni clusters and exhibit long time-on-stream stability for DRM. 2. Using passivating promoters. Promoters, such as S (Sulphur passivated steam reforming of methane, known as SPARG process) [21], K [7], Sn [22–24], Ag [25–27] and Au [28,29], are able to block the under-coordinated sites on Ni surfaces by forming surface alloy structure or being preferentially adsorbed on these sites, and are particularly effective to retard the nucleation of surface carbon species. Concomitantly, the blockage of more catalytically active under-coordinated sites significantly reduces the intrinsic activity of pristine Ni, through both geometric and electronic effects. 3. Adopting gasifying promoters or supports. Promoters such as Co [17,30,31], Ba [32], Ca [33,34], Fe [35–38] or supports like  $\text{La}_2\text{O}_3$  (by forming  $\text{La}_2\text{O}_2\text{CO}_3$  serving as  $\text{CO}_2$  pool) [39,40], ceria-zirconia oxides (acting as  $\text{CO}_2$  activation sites and oxygen pool) [41] can accelerate the gasification of surface carbon species without reducing the intrinsic activity of Ni. 4. Use combined strategies. For instance, Cr substituted Ni-MgO solid solution enhances

the catalyst stability for high pressure systems as a result of both small Ni size and Cr promoting effect [42].  $\text{SiO}_2$  encapsulated small Ni particles in addition to La promoter have recently been reported by Kawi et al. [43] to be effective to suppress carbon deposition. 5. Using noble metal promoters. Although the sole use of noble metal catalysts is costly, a small amount of noble metal promoter is possible. Indeed, Pt, Ru, and Rh enhance the long term stability of Ni in DRM has been observed [44–46], but the role noble metals play in the carbon-resistant property still entails further elucidation. In the context of anti-carbon catalyst development, the basic understanding of roles of promoters and construction of reliable structure-catalysis relationships are among the center guidance for catalyst design, for which more in-depth clarification is still needed.

Among these noble metals, Ru is relatively inexpensive and monometallic Ru is the very first metal to show activity and durability for DRM [47], with the reaction mechanism and kinetic behavior comparable to that of Ni [48]. Density Functional Theory (DFT) calculations predicted an oxygen affinity of Ru [9], which assists the gasification of surface carbon intermediates. More recently, theoretical modeling also suggests that Ru may bring about a desirable strain effect that will destabilize the carbon species over its surface [49], thus, facilitating the dynamic removal of carbon species. Numerous catalytic evaluations suggest that Ru could promote anti-coking property of pristine Ni [50–55], however, the effects of preparation caused structural complexity is often overlooked, and inconsistent results showing that Ru-Ni catalyst is ineffective to circumvent carbon deposition has also been reported [56]. Ni and Ru are immiscible and the bimetallic catalysts may exist largely as monometallic particles or mixed particles of distinct phases due to a strong segregation energy (for Ni(111) facet, 0.32 eV Ru-Ni segregation was inferred from DFT calculations) [56]. To find promoting effect of Ru, the structural complexity requires a careful examination of structural variations during catalyst preparation, catalytic assessments and for spent catalysts. Moreover, how and to which extent Ru alters carbon deposition or gasification rate, as well as how operation conditions like pressure and temperature influence these rates have not been well understood to the best of our knowledge. In view that carbon deposition is a dynamic process, there is no net carbon accumulation under conditions that carbon gasification overrates carbon deposition. Therefore, a fundamental understanding of the kinetics for carbon deposition and gasification processes is indispensable in the design of novel bimetallic catalysts and appropriate reactors.

Herein, we intend to shed light on the effect of Ru in Ni-MgO catalyzed DRM. The targets of this work are two folds. 1. To find the various factors that influence the composition, structure of Ru-Ni catalyst during preparation procedure and the corresponding catalytic consequences, as well as carbon-tolerant properties. 2. To understand the kinetic effect of Ru on rates of both carbon deposition and gasification in a quantitative way, and shed light on how operation conditions, such as feeding, pressure and temperature impact these rates.

## 2. Experimental section

### 2.1. Materials

Magnesium acetate tetrahydrate ( $\text{Mg}(\text{CH}_3\text{COO})_2 \cdot 4\text{H}_2\text{O}$ , AR), Nickel acetate tetrahydrate ( $\text{Ni}(\text{CH}_3\text{COO})_2 \cdot 4\text{H}_2\text{O}$ , AR) and methanol ( $\text{CH}_3\text{OH}$ , AR) were purchased from Sinopharm Chemical Reagent Co. Ltd. Ruthenium acetate ( $\text{Ru}(\text{CH}_3\text{COO})_x$ , 47 wt.% of Ru) was provided by Xiya Reagent.

### 2.2. Catalyst preparation

All chemicals were employed directly for the synthesis of catalysts without further purifications. The catalysts were prepared through a solvothermal synthesis that produced a single solid precipitate precursor, and a subsequent thermolysis of the precursor produced the

corresponding mixed oxides [57]. In a typical synthesis, methanol was stirred continuously for 2 h at 65 °C under N<sub>2</sub> bubbling in a flask to remove dissolved oxygen. During the synthesis process, Ru, Ni and Mg acetates with molar ratio of x:7-x:93 were dissolved in methanol to afford a homogeneous clear solution of 0.2 M (total metallic basis), which was left to stir continuously for 3 h before charged into a 200 ml Teflon-lined stainless steel autoclave and heated at 180 °C for 24 h in a convection oven. The solid educts were recovered by filtration, washed with methanol and dried in an oven at 70 °C for 12 h. To find the influence of pretreatment conditions on the structure of catalysts and the corresponding catalysts performance, two series Ru-Ni-MgO catalysts with varied metal compositions and different pretreatments were prepared from the intermediate. Parts of the intermediate was heated in a muffle oven to 800 °C in air via a ramp of 2 °C min<sup>-1</sup> for 6 h, which were denoted as Ru<sub>x</sub>Ni<sub>y</sub>Mg<sub>1-x-y</sub>O-C. Ru<sub>x</sub>Ni<sub>y</sub>Mg<sub>1-x-y</sub>O-C samples were reduced in H<sub>2</sub> flow of 30 ml min<sup>-1</sup> with a heating rate of 5 °C min<sup>-1</sup> to 800 °C, and soaked at 800 °C for 2 h, before being passivated in mixture gas of O<sub>2</sub> and Ar (1% O<sub>2</sub>, 30 ml min<sup>-1</sup>) at room temperature, which were labelled as Ru<sub>x</sub>Ni<sub>y</sub>Mg<sub>1-x-y</sub>O-CR, with suffix indicating calcination and reduction. Samples derived from direct reduction under H<sub>2</sub> atmosphere with identical conditions were passivated in the same O<sub>2</sub> and Ar (1% O<sub>2</sub>, 30 ml min<sup>-1</sup>), denoted as Ru<sub>x</sub>Ni<sub>y</sub>Mg<sub>1-x-y</sub>O-DR, with DR representing directly reduced.

### 2.3. Characterization techniques

Powder X-ray diffraction (XRD) patterns were recorded on a Rigaku D/Max-RC powder diffractometer using Cu K $\alpha$  radiation (operating at 40 kV and 100 mA,  $\lambda$  = 1.54178 Å). The diffractograms were collected in the 2 $\theta$  range 10–80° with a scan rate of 0.2° s<sup>-1</sup>.

Scanning Electronic Microscopic (SEM) images were recorded using a NOVA Nano SEM450 microscope equipped with a field emission gun made of tungsten wire. The powder was carefully dispersed on a conducting resin and evacuated at pressure of 2 mbar for 30 min before measurements. Distribution of all constituent elements was checked by elemental mapping using the same setup.

Transmission Electron Microscope (TEM) analyses were performed on a JEOL JEM-2100 instrument operated at 200 kV. The samples were prepared via dispersion in ethanol on 400 mesh copper grids pre-coated with thin carbon films. Pretreatment under ultrasonication was used to disperse the powder before each measurement. The metal particle size distribution was obtained by statistical analysis of assumed spherical metal particles from over 30 reduced particles in the TEM images by Nano Measurer 1.2 [58], according to the formula [9] below:

$$d_s = \frac{\sum n_i d_i^3}{\sum n_i d_i^2} \quad (6)$$

Where  $d_s$  is the statistic average size of particles measurable through TEM,  $n_i$  is the number of particles with diameter of  $d_i$ .

The specific surface areas were calculated by N<sub>2</sub> physisorption isotherm measurements using the standard Brunauer–Emmett–Teller (BET) model after measuring at –196 °C. Prior to the N<sub>2</sub> adsorption, all samples were subjected to degassing at 350 °C overnight (20 h) under vacuum (10<sup>-8</sup> atm) to remove the surface contaminants.

To check the reducibility of catalysts, H<sub>2</sub>-temperature programmed reduction (H<sub>2</sub>-TPR) of samples were collected in a Micromeritics Auto Chem II2920 instrument connected with an on-line thermal conductivity detector (TCD) that monitored H<sub>2</sub> consumption. Each fresh sample placed at the bottom of the U-shaped quartz tube was investigated by heating the samples from 20 °C to 900 °C in H<sub>2</sub> (5.0 vol. %)/Ar flow (30 ml min<sup>-1</sup>) with a ramp of 10 °C min<sup>-1</sup> and kept at 900 °C for 30 min till no H<sub>2</sub> consumption was detected.

X-ray photoelectron spectroscopy (XPS) was performed using a Thermo Fisher Scientific ESCALAB 250 spectrometer, using Al K $\alpha$  radiation (1486.8 eV, pass energy 30.0 eV) and recorded at  $\theta$  = 90° of X-

ray beams. The base pressure of the instrument was kept at 10<sup>-8</sup>–10<sup>-9</sup> Torr. The background contribution B (E) caused by inelastic processes was subtracted, and the curve fitting was performed with a Gaussian-Lorentzian profile (20% Gaussian and 80% Lorentzian) by the standard XPS PEAK 4.1 software. The binding energies (BEs) over supported catalysts were calibrated using the ubiquitous C1s peak at 284.6 eV.

Chemisorption was employed to determine the number of active sites for reduced catalysts, from which turn over frequency (TOF) numbers were generated. The measurements were conducted using CO titration. In each experiment, 100.0 mg of catalyst was used. The sample was heated to 800 °C in 10% H<sub>2</sub>/Ar with a flow rate of 30.0 mL min<sup>-1</sup>, ramped by a step of 5 °C min<sup>-1</sup> and kept there for 2 h. After reduction, the catalyst was purged with an ultra-high-purity helium (99.999%, Air Liquide Shanghai Co., Ltd.) flow before being cooled to room temperature. CO pulses were charged over the reduced catalyst and the CO uptake in each pulse was monitored using a TCD. Here the stoichiometry of CO to surface of Ni or Ru is 1.

Thermogravimetric analyses (TGA) were performed for spent catalysts to determine the type and amount of carbon deposition, using a thermogravimetric analyzer Pyris 1 TGA (Perkin Elmer) in successive CO<sub>2</sub> and air atmosphere. Under CO<sub>2</sub> atmosphere, gasifiable carbon amount was measured as recalcitrant carbon could not be oxidized by CO<sub>2</sub>. Samples were heated to 800 °C in CO<sub>2</sub> flow of 50 mL min<sup>-1</sup> at a rate of 10 °C min<sup>-1</sup> first to determine the amount of gasifiable carbon. The amount of residue recalcitrant carbon on spent catalysts was quantified by a subsequent TGA that was carried out under the air atmosphere, heating to 800 °C in air flow of 50 mL min<sup>-1</sup> at a rate of 10 °C min<sup>-1</sup>. By comparing the two values, it is possible to differentiate the types of carbon and evaluate the effect of Ru on the types of carbon formed during catalytic tests by comparing with un-promoted mono-metallic catalysts.

### 2.4. Catalytic assessments

The evaluation of catalytic performance was conducted in a fixed-bed reactor made of the quartz tube, whose inner diameter is 10 mm. Catalysts were pressed into pellets and sieved to 40–60 mesh before use. Typically, 0.035 g of catalyst was diluted with 1.00 g quartz sand (Shanghai Ling Feng chemical reagents Co., Ltd.) of the same particle size. The mixture of catalyst and quartz sand was supported by quartz wool in the reactor. Before reaction, the mounted catalyst was reduced in situ by high-purity H<sub>2</sub> (60 mL min<sup>-1</sup>, 800 °C) for 2 h prior to the catalytic reaction. The evaluation of the catalysts was carried out at 760 °C or 800 °C under 1 atm, respectively. All the gas cylinders were provided by Shanghai Dumao Air Purified Gas Co. Ltd., with a purity of 99.9999% for H<sub>2</sub>, CH<sub>4</sub>, and N<sub>2</sub> and 99.995% CO<sub>2</sub>. Prior to catalytic test, a blank test was carried out and no activity was detected without catalyst. The feed gas flow rate to the reactor was set at 50 mL min<sup>-1</sup> (GHSV  $\approx$  86,000 mL h<sup>-1</sup> g-cat<sup>-1</sup>), with a stoichiometric feeding ratio of CH<sub>4</sub>:CO<sub>2</sub> = 25:25 under harsh diluent-gas free reaction conditions. The time-on-stream tests were carried out at CH<sub>4</sub> conversion levels below thermodynamic equilibrium conversion, so as to avoid the artifacts and ensure that the measurements were reflecting the intrinsic activity of catalysts.

The effluent gas was analyzed by GC-9860 (Shanghai Qi Yang Instrument), equipped with a TDX-01 column and an on-line TCD. CH<sub>4</sub>, CO<sub>2</sub> conversion ( $X_{\text{CH}_4}$  and  $X_{\text{CO}_2}$ ), selectivity to H<sub>2</sub> and CO ( $S_{\text{H}_2}$  and  $S_{\text{CO}}$ ), and the H<sub>2</sub>/CO ratio are defined as follows:

$$X_{\text{CH}_4} = \frac{F_{\text{CH}_4,\text{in}} - F_{\text{CH}_4,\text{out}}}{F_{\text{CH}_4,\text{in}}}, X_{\text{CO}_2} = \frac{F_{\text{CO}_2,\text{in}} - F_{\text{CO}_2,\text{out}}}{F_{\text{CO}_2,\text{in}}} \quad (7)$$

$$S_{\text{H}_2} = \frac{F_{\text{H}_2,\text{out}}}{(F_{\text{CH}_4,\text{in}} - F_{\text{CH}_4,\text{out}}) + (F_{\text{CO}_2,\text{in}} - F_{\text{CO}_2,\text{out}})} \quad (8)$$

$$S_{CO} = \frac{F_{CO_2,out}}{(F_{CH_4,in} - F_{CH_4,out}) + (F_{CO_2,in} - F_{CO_2,out})} \quad (9)$$

$$H_2/CO = \frac{S_{H_2}}{S_{CO}} \quad (10)$$

Where  $F_{CH_4,in}$ ,  $F_{CO_2,in}$ ,  $F_{CH_4,out}$ ,  $F_{CO_2,out}$ ,  $F_{CO,out}$  and  $F_{H_2,out}$  are the inlet flow rates for  $CH_4$ ,  $CO_2$ , the effluent flow rates for  $CH_4$ ,  $CO_2$ ,  $CO$  and  $H_2$ , respectively.

## 2.5. Kinetic studies

To investigate the effect of Ru-Ni on activation energies, kinetic experiments were carried out for monometallic Ni, Ru and bimetallic catalysts, with a diluted feed gas molar ratio of  $CH_4:CO_2:N_2 = 25:25:18$  at 1 atm total pressure in the temperature ranging from 500 °C to 700 °C, respectively. For each test, 10 mg catalyst sieved to 40–60 mesh was diluted with 1.00 g quartz sand, mounted in the reactor, before reduced in  $H_2$  for 2 h. The influence of both internal diffusion and external diffusion to kinetic studies was strictly ruled out according to [25,48]. The conversion levels were kept below 10% to avoid the effect of reverse reaction.

Forward turnover rates ( $r_f$ ) are given by [8]:

$$r_f = r_n/(1 - \eta) \quad (11)$$

Where  $r_n$  is the net  $CH_4$  conversion turnover rate,  $\eta$  is the approach to equilibrium which is given by [8]:

$$\eta = \frac{[P_{CO}]^2 [P_{H_2}]^2}{[P_{CH_4}] [P_{CO_2}]} \times \frac{1}{K} \quad (12)$$

$K$  is equilibrium constant for dry reforming,  $P_{CO}$ ,  $P_{H_2}$ ,  $P_{CH_4}$  and  $P_{CO_2}$  are the partial pressures for a given reaction condition.

To investigate the reaction order for  $CH_4$  and  $CO_2$  on  $Ni_{0.07}Mg_{0.93}O$ ,  $Ru_{0.003}Ni_{0.067}Mg_{0.93}O$ ,  $Ru_{0.07}Mg_{0.93}O$ , reaction rate dependence on  $CH_4$  and  $CO_2$  partial pressures were conducted with a feed gas flow rate to the reactor of  $93 \text{ mL min}^{-1}$  at 760 °C. Partial pressures of  $CH_4$  or  $CO_2$  were manipulated between 27 kPa and 70 kPa or from 30 kPa to 73 kPa, and the total pressure and the flow rate were made up by diluent gas  $N_2$ .

A method for determining the (eff ;ective of promoter on) carbon gasification rate by using  $CO_2$  oxidation of deposited carbon over spent catalysts was proposed as follows, which was based on a modified Wigner–Polanyi equation (often used to generate kinetic data for TPD process) [59]. As only small amount of surface carbon was identified on spent catalysts, and most of which can be gasified by  $CO_2$  via reverse Boudouard reaction (reaction 13) to  $CO$ , by assuming that the reverse reaction and re-adsorption are negligible, the following gasification kinetic law (Eq. (14)) applies to the  $CO_2$  surface gasification process [60,61]. The effect of  $CO_2$  desorption can be ruled out as platelet-shaped NiMgO is enclosed by (111) facets that are made up of alternating  $Mg^{2+}$  cations and  $O^{2-}$  anions, which desorbs  $CO_2$  at temperatures as low as 223 °C [57]. These conditions are satisfied under our  $CO_2$ -excessive  $CO_2$ -TPO conditions operating under the high flow rate of carrier gas (He,  $30 \text{ mL min}^{-1}$ ), and first order reaction to surface carbon concentration was identified before [60].



$$r = -\frac{d\theta^*}{dt} = A\theta^* \exp\left[-\frac{E_a}{RT}\right] p_{CO_2}^n \quad (14)$$

Where  $A$  is the pre-exponential factor,  $\theta^*$  is the surface carbon coverage,  $E_a$  is the activation energy and  $n$  is the reaction order with respect to  $CO_2$  partial pressure.  $R$  and  $T$  are the universal gas constant and temperature, respectively. To determine the kinetic parameters,  $A$ ,  $n$  and  $E_a$  need to be identified by regression. Prior to the  $CO_2$ -TPO measurements,  $Ni_{0.07}Mg_{0.93}O$ -DR and  $Ru_{0.003}Ni_{0.067}Mg_{0.93}O$ -DR were deliberately coked with a gas molar ratio of  $CH_4:CO_2 = 25:25$  at 1 atm

total pressure at 800 °C for 24 h, in order to collect enough spent samples for kinetic studies using  $CO_2$ -TPO technique. All samples were outgassed to 120 °C to remove surface contaminants during post-tests handlings under  $N_2$  for 1 h, such as water. In the first series experiments, we used a tiny amount of spent catalysts (typically 50 mg) and a pure flow of  $CO_2$ , in order that the concentration variation of  $CO_2$  can be deemed as constant. The samples placed at the bottom of the U-shaped quartz tube were investigated by heating the samples from 30 °C to 800 °C in  $CO_2$  (100 vol.%) flow ( $30 \text{ mL min}^{-1}$ ) at heating rates of 5, 7.5, 10, 12.5, 15 °C  $\text{min}^{-1}$ , respectively. The  $CO_2$  consumption was monitored by a TCD. Under such circumstances, a pseudo zeroth kinetic order for  $P_{CO_2}$  applies, and  $E_a$  could therefore be measured by changing ramp of heating for  $CO_2$ -TPO,

$$r = -\frac{d\theta^*}{dt} = A\theta^* \exp\left[-\frac{E_a}{RT}\right] p_{CO_2}^n = A p_{CO_2}^n \theta^* \exp\left[-\frac{E_a}{RT}\right] \quad (15)$$

$A p_{CO_2}^n$  can be regarded as an invariable, for the exceedingly high partial pressure and small consumption.

During the TPO analysis, the temperature is increased linearly by:

$$T_i = T_0 + \beta t \quad (16)$$

Where  $\beta = dT/dt$  and  $T_0$  is the initial temperature. Thus:

$$-\frac{d\theta^*}{dT} \beta = A p_{CO_2}^n \theta^* \exp\left[-\frac{E_a}{RT}\right] \quad (17)$$

If  $T_M$  is the maximum temperature of a given TPO spectrum, then:

$$\frac{d}{dT} \left[ \theta^* \left( \frac{A p_{CO_2}^n}{\beta} \right) \exp\left(\frac{E_a}{RT}\right) \right]_{T_M} = 0 \quad (18)$$

$$\beta E_a = R T_M^2 A p_{CO_2}^n \exp\left(-\frac{E_a}{R T_M}\right) \quad (19)$$

$$\ln\left(\frac{T_M^2}{\beta}\right) = \frac{E_a}{R T_M} + \ln\left(\frac{E_a}{A p_{CO_2}^n R}\right) \quad (20)$$

$$2 \ln T_M - \ln \beta = \frac{E_a}{R T_M} + \ln\left(\frac{E_a}{A p_{CO_2}^n R}\right) \quad (21)$$

$2 \ln T_M - \ln \beta$  vs.  $1/T_M$  curve can be used to deduce  $E_a$  from the slope,  $A$  could also be inferred for a known  $A p_{CO_2}^n$ .

Next, to determine  $n$ , a small amount of spent catalysts (25 mg) were investigated by heating from 30 °C to 800 °C in varied  $P_{CO_2}$  (100, 50, 26.7, 13.3, 6.7 vol.%) / He flow (The total flow was  $30 \text{ mL min}^{-1}$ ) at the same ramp of  $10^\circ \text{C min}^{-1}$ . Both reaction order  $n$  and pre-exponential factor  $A$  can be calculated from Eq. (22) by plotting  $\ln\left(\frac{T_M^2}{\beta}\right) - \frac{E_a}{R T_M}$  against  $\ln P_{CO_2}$ , from the slope and intercept, respectively.

$$2 \ln T_M - \ln \beta - \frac{E_a}{R T_M} - \ln E_a + \ln A R = -n \ln P_{CO_2} \quad (22)$$

## 3. Results and discussion

### 3.1. Catalyst preparation and pretreatment

$Ru_xNi_yMg_{1-x-y}O$  catalysts were prepared by a solvothermal synthesis developed by some of us [17,57], via the formation of  $Ru_xNi_yMg_{1-x-y}(OH)(OCH_3)$  as the precursor and its topotactic thermolysis. The merits of such a preparation include that the metal loadings, their even distribution and surface structure can be controlled at the beginning of catalyst preparation. As Ni-MgO is a carbon-resistant catalyst for DRM at low Ni loadings [62], it is important to increase Ni loading to a level that the pristine Ni-MgO catalyst cokes such that the effect of Ru could be exaggerated. From XRD patterns for the as-synthesized intermediates (Fig. S1, Supporting information), it is found that for  $Ru_{0.07}Mg_{0.93}(OH)(OCH_3)$  or  $Ru_xNi_yMg_{1-x-y}(OH)(OCH_3)$  with  $x + y < 7 \text{ mol.}\%$ ,  $Ru^{2+}$  can



be incorporated into  $M(OH)(OCH_3)$  structure via isomorphous substitution, for which  $M = Mg^{2+}$ ,  $Ni^{2+}$ ,  $Mn^{2+}$ ,  $Co^{2+}$ , or other cations [17,63,64]. The introduction of Ru at low loadings does not cause observable Ru reduction or segregation. A prominent diffraction intensity for diffraction from (001) is a typical fingerprint for such a structure, which also recommends anisotropic growth of the  $R\bar{3}m$  crystal. Infrared (IR) spectra of the typical sample is identical to  $Mg(OH)(OCH_3)$  or  $Ni(OH)(OCH_3)$ , further corroborating the structure is intact with the charging of Ru (Fig. S2). SEM and the corresponding elemental mapping certifies that Ru, Ni and Mg are homogeneously distributed (Fig. S3). TEM images and Selected Area Electron Diffraction (SAED) patterns for the  $Ru_{0.07}Mg_{0.93}(OH)(OCH_3)$  and  $Ru_{0.003}Ni_{0.067}Mg_{0.93}(OH)(OCH_3)$  samples suggest that the platelet is perpendicular to the (001) facets of the  $R\bar{3}m$  structure (Fig. S4). Briefly, solvothermal synthesis produced multi-component catalyst precursors with well controlled platelet-like shape, orientation, and homogeneously distributed metals as single source precursor.

To examine the influence of pretreatment conditions on the structure of catalysts, the precursors  $Ru_xNi_yMg_{1-x-y}(OH)(OCH_3)$  were subjected to different pretreatments. Samples that were calcined in air were labelled as  $Ru_xNi_yMg_{1-x-y}O-C$ , with the suffix indicating calcined. Samples derived after reduction of  $Ru_xNi_yMg_{1-x-y}O-C$  in  $H_2$  were denoted as  $Ru_xNi_yMg_{1-x-y}O-CR$ , with suffix indicating calcined and subsequently reduced. For comparison, another series of samples, prepared via direct reduction of  $Ru_xNi_yMg_{1-x-y}(OH)(OCH_3)$  precursors in  $H_2$ , were named as  $Ru_xNi_yMg_{1-x-y}O-DR$ , whereby DR representing directly reduced. The XRD patterns for  $Ru_xNi_yMg_{1-x-y}O-C$ ,  $Ru_xNi_yMg_{1-x-y}O-CR$  and  $Ru_xNi_yMg_{1-x-y}O-DR$  are shown in Fig. 1a–c, respectively. For  $Ni_{0.07}Mg_{0.93}O-C$  and  $Ru_{0.003}Ni_{0.067}Mg_{0.93}O-C$ , only diffraction lines stemming from  $NiO$ - $MgO$  solid solution can be discerned, showing that Ruthenium oxide dissolves in the solids solution at such low loadings. In contrast, for  $Ru_{0.035}Ni_{0.035}Mg_{0.93}O-C$  and  $Ru_{0.07}Mg_{0.93}O-C$ , it is observed that the calcination step has incurred partial segregation of  $RuO_2$  as a separate phase for both samples. The segregation is indicative of the facile change of valence number for  $Ru^{2+}$  upon exposure to high temperature calcination in air.  $RuO_2$  has a tetragonal structure (JCPDS No. 40-1290) that is different from rocksalt structure of  $NiO$ - $MgO$  solid solution, which incurred the phase segregation when Ru loading is high.

SEM and TEM images for representative  $Ru_{0.003}Ni_{0.067}Mg_{0.93}O-C$  are shown in Fig. S5. SEM images disclose that the sample is made up of porous platelets, confirming that the platelet shape was preserved during the calcination process. The platelet has a typical thickness of 29 nm and a lateral size between 1.20 and 1.96  $\mu m$ , and the mapping results show that all constituent elements are uniformly distributed in the sample. Thermolysis of alike precursor  $Mg(OH)(OCH_3)$ ,  $Ni_xMg_{1-x}(OH)(OCH_3)$  in the series material was found to be a topotactic transformation, whereby the (001) facets along the normal of platelet was converted into a rocksalt structured solid solution exposing (111) facets [17,62,64]. For the Ru containing  $Ru_{0.003}Ni_{0.067}Mg_{0.93}O-C$  precursors, the same topotactic transformation might have occurred. To prove this hypothesis, TEM images and a corresponding SAED were collected, as displayed in Fig. S5. The porous feature was a result of lattice shrinkage in the thermolysis process, and the SAED observed perpendicular to the platelet corroborates that the surface is enclosed by (111) surface as expected.

When the calcined samples were reduced in  $H_2$ ,  $Ni_{0.07}Mg_{0.93}O-CR$  and  $Ru_{0.003}Ni_{0.067}Mg_{0.93}O-CR$  exhibited identical XRD patterns (Fig. 1b). An additional reflection line attributable to  $Ni^0$  phase could be identified, showing that both metals in the samples were reduced to Ru-Ni alloy, no segregation was perceivable via XRD. From the phase diagram, it is seen that Ni and Ru are immiscible, and can form a Ni-rich phase only when Ru content is less than 7 mol.% at temperatures above 800 °C [65], which was also confirmed by a recent study by Morales-Cano et al. [56]. For  $Ru_{0.035}Ni_{0.035}Mg_{0.93}O-CR$  and  $Ru_{0.07}Mg_{0.93}O-CR$ , another Ru-rich phase (JCPDS No. 06-0663) was found, implying the

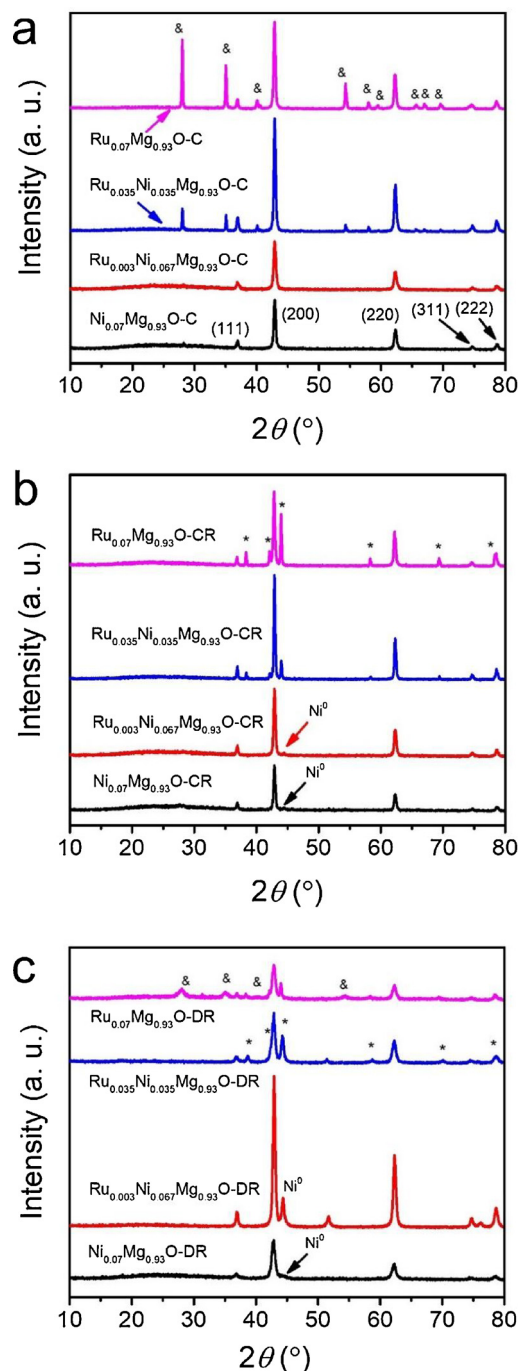


**Fig. 1.** XRD patterns for the three series samples: (a)  $Ru_xNi_yMg_{1-x-y}O-C$  samples after calcination of precursors  $Ru_xNi_yMg_{1-x-y}(OH)(OCH_3)$  at 800 °C for 6 h in air, (b)  $Ru_xNi_yMg_{1-x-y}O-CR$  samples after reduction of  $Ru_xNi_yMg_{1-x-y}O-C$  in  $H_2$  flow of 30 ml min<sup>-1</sup> at 800 °C for 2 h, and (c)  $Ru_xNi_yMg_{1-x-y}O-DR$  samples derived after direct reduction of precursors  $Ru_xNi_yMg_{1-x-y}(OH)(OCH_3)$  in  $H_2$  flow of 30 ml min<sup>-1</sup> at 800 °C for 2 h. \*Indicates diffractions from Ru particles (JCPDS No. 06-0663,  $2\theta = 38.4, 42.2, 44.0, 58.3, 69.4, 78.4$ ). & shows diffractions out of  $RuO_2$  (JCPDS No. 40-1290,  $2\theta = 28.0, 35.1, 40.0, 40, 54.2, 58.0, 59.4, 65.5, 65.9, 67.0$ ).  $Ni^0$  (JCPDS No. 04-0850,  $2\theta = 44.5, 51.8, 76.4$ ).

very limited range for Ru-Ni alloy variation.

The XRD patterns for samples obtained by direct reduction of precursors,  $Ru_{0.003}Ni_{0.067}Mg_{0.93}O-DR$  and  $Ru_{0.035}Ni_{0.035}Mg_{0.93}O-DR$  are compared with the monometallic samples in Fig. 1c. The reduced  $Ni_{0.07}Mg_{0.93}O-DR$  shows a weak diffraction from metallic  $Ni^0$ , while the  $Ru_{0.003}Ni_{0.067}Mg_{0.93}O-DR$  displays a strong intensity of diffraction from

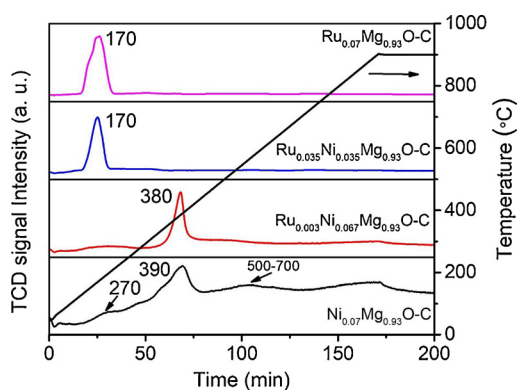


Fig. 2.  $H_2$ -TPR patterns for samples  $Ru_xNi_{0.07-x}Mg_{0.93}O-C$  after calcination of precursors  $Ru_xNi_{0.07-x}Mg_{0.93}(OH)(OCH_3)$ , with a ramp of  $10\text{ }^\circ\text{C min}^{-1}$  from  $25\text{ }^\circ\text{C}$  to  $900\text{ }^\circ\text{C}$  and  $H_2$  flow rate of  $30\text{ ml min}^{-1}$ .

$Ni^0$ , suggesting that the presence of Ru has promoted the reduction of Ni in the solid solution, as  $RuO_2$  can be more facily reduced than  $NiO$ . For  $Ru_{0.035}Ni_{0.035}Mg_{0.93}O-DR$ , since the Ru loading exceeds the miscible limit, a separate Ru-rich phase can also be seen. For monometallic counterpart,  $Ru_{0.07}Mg_{0.93}O-DR$ , both metallic  $Ru^0$  and  $RuO_2$  were detected by XRD, suggesting a disproportionation of  $Ru^{2+}$  in the solid solution occurred even in the highly reducing  $H_2$  atmosphere. Normally,  $RuO_2$  can easily be reduced by  $H_2$  [66], nonetheless, herein, the preparation of  $Ru_{0.07}Mg_{0.93}O-DR$  was accompanied by the thermal decomposition of  $Ru_{0.07}Mg_{0.93}(OH)(OCH_3)$ , which might have complicated the process. To sum up, pretreatment of the same precursor actually ended up with samples of diversified composition and phases, manifesting that the Ru-Ni system is highly sensitive towards pretreatment condition variations. The dependence of structure and composition upon treating conditions and precursor composition were not carefully examined before. The textural properties of the two series of pretreatment catalysts are shown in Table S1.

$H_2$ -TPR was employed to probe the reducibility of the precursor  $Ru_xNi_yMg_{1-x-y}(OH)(OCH_3)$  and the calcined  $Ru_xNi_yMg_{1-x-y}O-C$  samples, as displayed in Figs. S6a and Figure 2, respectively. Monometallic  $Ni_{0.07}Mg_{0.93}O-C$  exhibits a major reduction peak at  $390\text{ }^\circ\text{C}$  in addition to a low temperature shoulder peak at ca.  $270\text{ }^\circ\text{C}$ . The rather weak low temperature reduction peak at  $200\text{--}270\text{ }^\circ\text{C}$  is associated with  $Ni^{3+}$  surface species locate at surface sites [67] or the surface oxygen reduction in  $NiMgO(111)$  platelets [64]. The reduction peak centered at  $380\text{--}390\text{ }^\circ\text{C}$  can be ascribed to the reduction of outermost and sublayer  $Ni^{2+}$  that interacts strongly with the Ni-MgO solid solution [68]. Embedded  $NiO$  interacting strongly with sublayer solid solution is only reducible at temperatures ranging from  $500\text{ }^\circ\text{C}$  to  $700\text{ }^\circ\text{C}$  [67], with a rather broad reduction profile. All  $Ru_xNi_yMg_{1-x-y}O-C$  bimetallic samples present essentially a single major reduction peak, whose position shows a systematic shift towards lower temperatures with the increase of Ru loading, which is in line with previous reports [51,53]. Interestingly,  $Ru_{0.003}Ni_{0.067}Mg_{0.93}O-C$  shows a major reduction peak at  $380\text{ }^\circ\text{C}$  close to monometallic  $Ni_{0.07}Mg_{0.93}O-C$  ( $390\text{ }^\circ\text{C}$ ), while the reduction temperature for  $Ru_{0.035}Ni_{0.035}Mg_{0.93}O-C$  ( $170\text{ }^\circ\text{C}$ ) resembles that for  $Ru_{0.07}Mg_{0.93}O-C$  ( $170\text{ }^\circ\text{C}$ ). Considering the rather lower reduction maximum for bimetallic catalysts with respect to the monometallic  $Ni_{0.07}Mg_{0.93}O-C$  catalyst, it is reasonable to conclude that Ru and Ni are in close contact and there is strong interaction between them. The shift is speculated to arise from a stronger oxygen affinity for Ru with respect to Ni, as the reduction of  $RuO_2$  at temperatures as low as  $100\text{--}120\text{ }^\circ\text{C}$  has been observed by Jakobsen et al. [69].

$H_2$ -TPR pattern of monometallic  $Ni_{0.07}Mg_{0.93}(OH)(OCH_3)$  precursor (Fig. S6a) shows one reduction peak at ca.  $380\text{ }^\circ\text{C}$ , corresponding to the reduction of  $Ni^{2+}$  to metallic  $Ni^0$  according to the XRD before and after reduction (Figs. S1 and Figure 1c). As the reduction of  $Ni_{0.07}Mg_{0.93}(OH)$

$(OCH_3)$  is complicated by the concurrent thermal decomposition, the reduction profile appears rather broad, and a contribution from thermolysis interfered the measurements (Fig. S6b). With the increase of Ru content in  $Ru_xNi_yMg_{1-x-y}(OH)(OCH_3)$ ,  $H_2$  consumption peak overlaps with disproportionation of Ru species, and a contribution from Ru oxidation counteracts  $H_2$  consumption, resulting in a barely distinguishable complex pattern. The intertwined thermolysis and reduction were particularly obvious for  $Ru_{0.07}Mg_{0.93}(OH)(OCH_3)$ , suggesting a simultaneous decomposition of precursor and reduction of Ni and part of Ru, which agrees well with the XRD observation for  $Ru_{0.07}Mg_{0.93}O-DR$  (Fig. 1c).

To reveal the influence of pretreatment conditions on the microscopic structure, TEM micrographs were obtained for reduced  $Ru_{0.07}Mg_{0.93}O-CR$ ,  $Ru_{0.003}Ni_{0.067}Mg_{0.93}O-CR$  and compared with the ones obtained from direct reduction of precursors, i.e.,  $Ru_{0.07}Mg_{0.93}O-DR$  and  $Ru_{0.003}Ni_{0.067}Mg_{0.93}O-DR$  (Fig. 3). The platelet shape of  $Ru_{0.07}Mg_{0.93}O-CR$  is maintained in the reduction process, and part of the solid solution has been reduced to tiny spherical shaped metallic particles that are situated on the sample surface. Further analyses of particle size distribution based on statistical calculations are manifested in the corresponding insets in histogram, obviously, a mean size of Ru centered at  $3\text{ nm}$ , ranging from  $2\text{ to }5\text{ nm}$ , can be calculated. The Ru particle size is smaller than Ni in reduced Ni-MgO solid solution (ca.  $7\text{ nm}$ ) [64], possibly because Ru can be reduced at a much lower temperature than Ni. In  $Ru_{0.07}Mg_{0.93}O-DR$  sample, the disproportionation of  $Ru^{2+}$  in the precursor produced randomly distributed larger  $15\text{--}30\text{ nm}$   $RuO_2$  particle, in addition to some metallic  $Ru^0$  that were finely dispersed and is beyond the detection limit of TEM technique. For  $Ru_{0.003}Ni_{0.067}Mg_{0.93}O-CR$ , there are both small and large metallic particles that can be detected, with average sizes of  $2.5\text{ nm}$  and  $8\text{ nm}$ , respectively. The diverse size may origin from the calcination and sequential reduction treatment, as the former caused the formation of a separate  $RuO_2$  phase that can be reduced to bigger particles and the latter could contribute to the formation of  $Ru^0$  that is hardly visible in XRD or TEM measurements. In contrast,  $Ru_{0.003}Ni_{0.067}Mg_{0.93}O-DR$  contains a narrow size distribution centered at  $5.5\text{ nm}$ , for which a simultaneous reduction of both  $RuO_x$  and  $NiO$  out of the precursor occurred. One may conclude from the comparisons that the direct reduction of the precursor with low Ru loading into the corresponding bimetallic catalyst is advantageous in terms of maintaining metal distribution and a narrow particle size distribution. Relatively small metallic particles have been produced with respect to monometallic Ni sample.

### 3.2. Catalytic performance

The catalytic performance of samples was evaluated at  $760$  and  $800\text{ }^\circ\text{C}$  under harsh diluent-gas free feeding conditions, with the intention to reflect the influence of pretreatment conditions on the structure and composition of catalysts, as well as the catalytic consequences. Comparisons were made with monometallic  $Ni_{0.07}Mg_{0.93}O$  and  $Ru_{0.07}Mg_{0.93}O$  catalysts and the conversion levels were kept below equilibrium conversions. The catalytic activities of  $Ru_xNi_yMg_{1-x-y}O-CR$  series at  $760\text{ }^\circ\text{C}$ ,  $CH_4/CO_2 = 1$ ,  $GHSV = 86,000\text{ ml h}^{-1}\text{ g-cat}^{-1}$  are displayed in Fig. 4a and c in terms of  $CH_4$  and  $CO_2$  conversion as a function of time-on-stream, and the corresponding selectivity expressed as  $H_2/CO$  ratio variation over the same measurements was manifested in Fig. 4e. For pristine  $Ni_{0.07}Mg_{0.93}O-CR$  catalyst, a high initial  $CH_4$  conversion of  $79\%$  was measured, which declined over time slowly, and ended up with a conversion of  $70\%$  after  $100\text{ h}$ . For monometallic  $Ru_{0.07}Mg_{0.93}O-CR$  catalyst, conversely, a low  $CH_4$  conversion of  $36\%$  was observed, but a subsequent increase in activity was found, and by the end of the  $100\text{ h}$  test, a conversion of  $70\%$  was deduced. The bimetallic samples,  $Ru_{0.035}Ni_{0.035}Mg_{0.93}O-CR$  and  $Ru_{0.003}Ni_{0.067}Mg_{0.93}O-CR$  demonstrated lower initial activities.  $Ru_{0.035}Ni_{0.035}Mg_{0.93}O-CR$  had virtually no activity in the first  $15\text{ h}$ , and slowly gained activity with



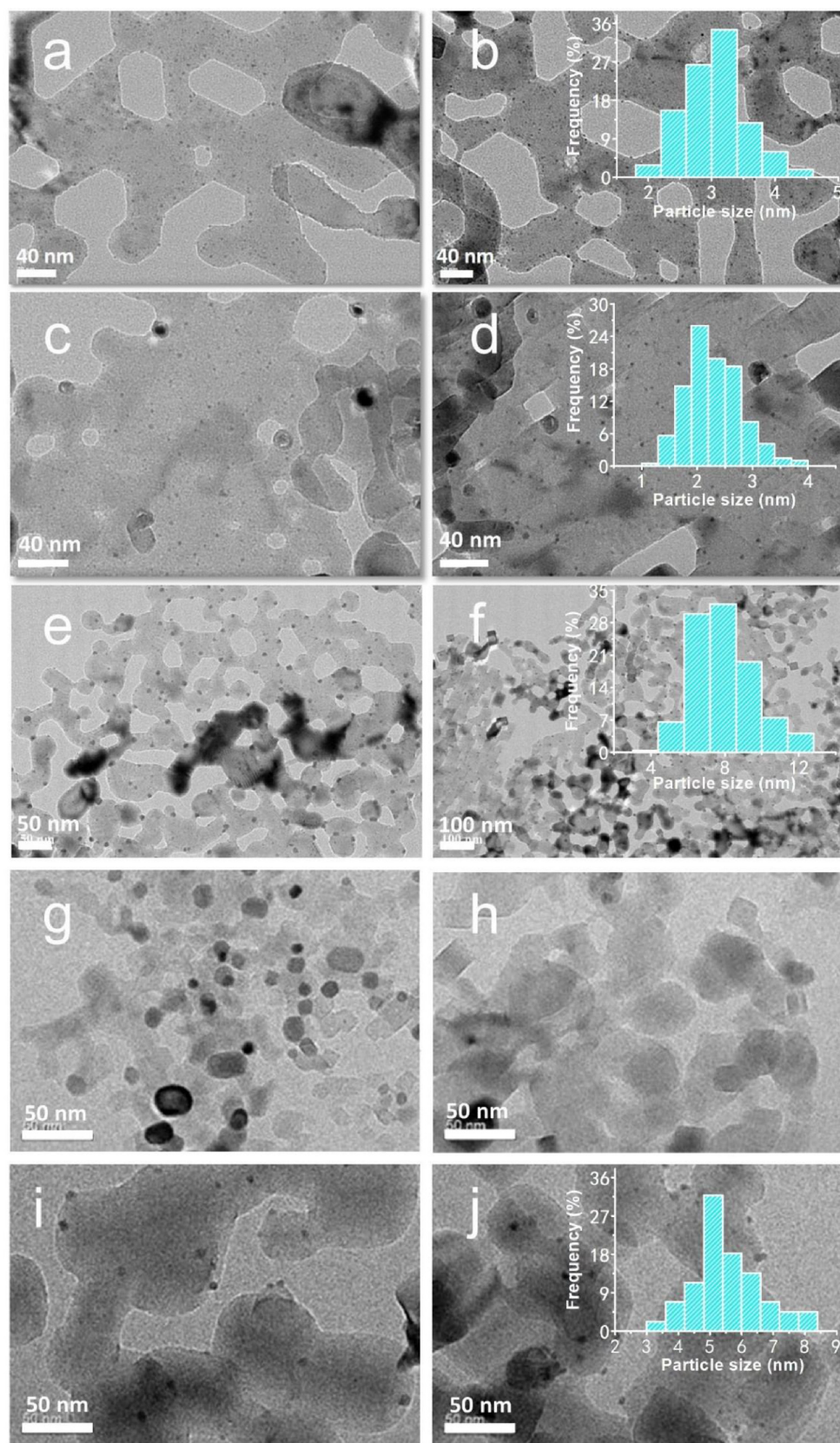


**Fig. 3.** TEM micrographs and particle size distribution of reduced metallic particles for (a, b) Ru<sub>0.07</sub>Mg<sub>0.93</sub>O-CR, (c, d) Ru<sub>0.003</sub>Ni<sub>0.067</sub>Mg<sub>0.93</sub>O-CR, (e, f) Ru<sub>0.003</sub>Ni<sub>0.067</sub>Mg<sub>0.93</sub>O-DR, (g, h) Ru<sub>0.07</sub>Mg<sub>0.93</sub>O-DR and (i, j) Ru<sub>0.003</sub>Ni<sub>0.067</sub>Mg<sub>0.93</sub>O-DR.

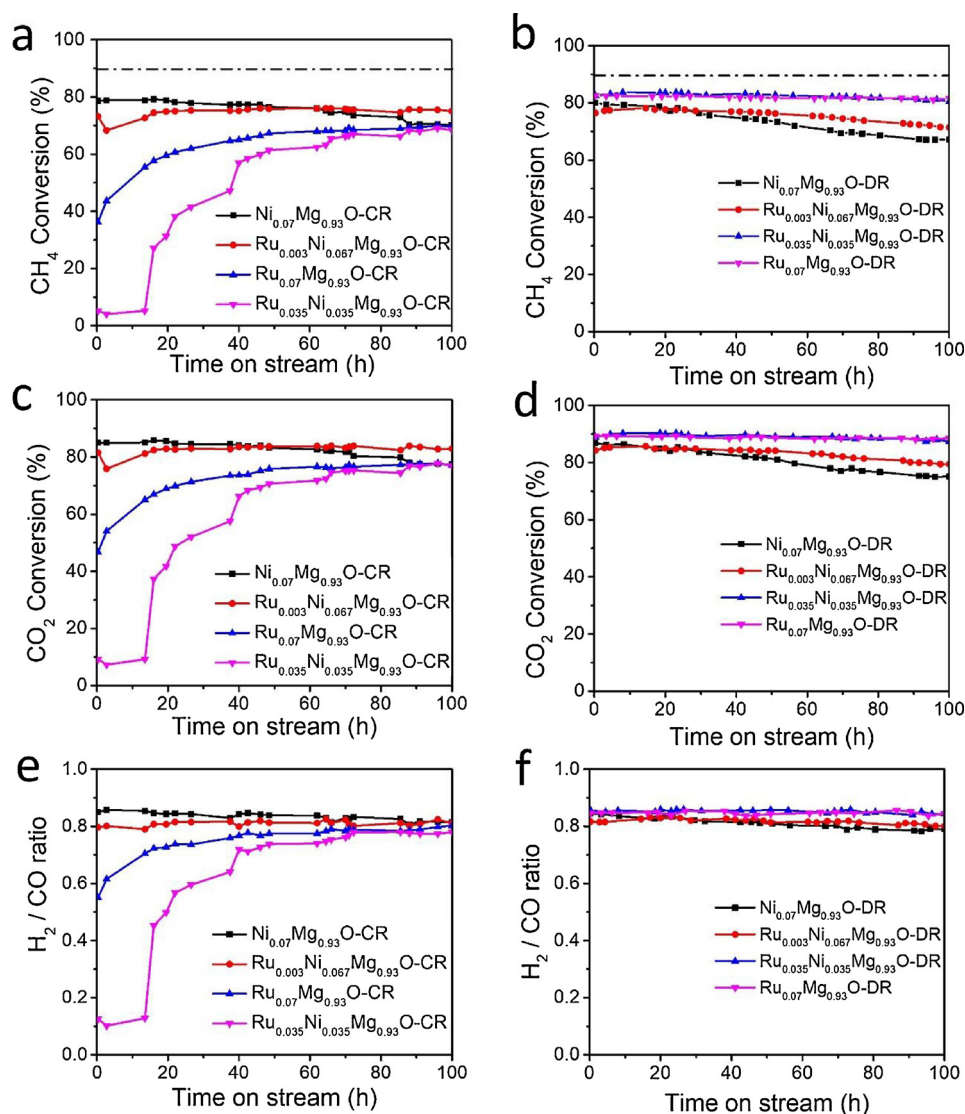
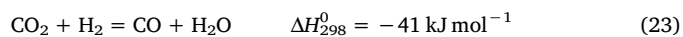


**Fig. 4.** Time-on-stream stability of Ru<sub>x</sub>Ni<sub>0.07-x</sub>Mg<sub>0.93</sub>O-CR (a, c) and Ru<sub>x</sub>Ni<sub>0.07-x</sub>Mg<sub>0.93</sub>O-DR (b, d) catalysts at 760 °C; CH<sub>4</sub> conversion (a, b), CO<sub>2</sub> conversion (c, d) and the corresponding H<sub>2</sub>/CO ratio variation (e, f). Reaction conditions: flow rates, CH<sub>4</sub> = 25 ml min<sup>-1</sup>, CO<sub>2</sub> = 25 ml min<sup>-1</sup>; pressure = 1.0 atm; GHSV = 86,000 mL h<sup>-1</sup> g-cat<sup>-1</sup>; catalyst weight = 0.035 g. The dashed line indicates equilibrium conversion of CH<sub>4</sub>.

elapsed time before reaching a steady state activity of 68% CH<sub>4</sub> conversion. Ru<sub>0.003</sub>Ni<sub>0.067</sub>Mg<sub>0.93</sub>O-CR exhibited an even lower initial activity with respect to pristine Ni<sub>0.07</sub>Mg<sub>0.93</sub>O-CR sample, whereas a steady state conversion of around 75% was attained within 30 h, and the activity remained constant for the rest of the test, ending up with a conversion of 75%. For all the tests, a higher CO<sub>2</sub> conversion level was inferred with respect to CH<sub>4</sub> conversion, showing that the concurrent RWGS had taken place that consumed H<sub>2</sub> and CO<sub>2</sub> to produce H<sub>2</sub>O and CO (reaction 23). The results also demonstrate that the introduction of Ru causes an abrupt decrease in initial activity if the samples were prepared by calcination-reduction route. The drastic activity loss indicates that the catalyst surface underwent oxidation in contact with the reacting atmosphere. As Ru is capable of activating CO<sub>2</sub> and being oxidized in exposure to CO<sub>2</sub> [70,71], which could cause surface oxidation of Ru-Ni particles and consequent activity loss. Upon exposing to CO<sub>2</sub>, an adsorption induced surface segregation with surface-rich Ru might have taken place. Surface oxygen coverage could block active sites until being reduced by H<sub>2</sub> derived from kinetically slow CH<sub>4</sub> dissociation [8]. This speculation is plausible as Ru was theoretically predicted to be oxyphilic [9], and CO<sub>2</sub> activation is kinetically less demanding than CH<sub>4</sub> over Ni or Ru surface [8,48]. Under steady state

operation, the presence of H<sub>2</sub> kept contacting atmosphere highly reducing, and preserved the samples in their metallic state. No significant deactivation was measured during the rest test.



In contrast, Ru<sub>x</sub>Ni<sub>y</sub>Mg<sub>1-x-y</sub>O-DR catalysts exhibited the highest initial activity (Fig. 4b), which gradually deactivated during the time-on-stream assessments. Monometallic Ru<sub>0.07</sub>Mg<sub>0.93</sub>O-DR (CH<sub>4</sub> conversion dropped from initial 83% to final 81%) showed improved time-on-stream stability than that of Ni<sub>0.07</sub>Mg<sub>0.93</sub>O-DR (CH<sub>4</sub> conversion declined from 80% to 67%). Ru<sub>0.035</sub>Ni<sub>0.035</sub>Mg<sub>0.93</sub>O-DR demonstrated comparable activity and stability to that of Ru<sub>0.07</sub>Mg<sub>0.93</sub>O-DR, only slight decrease (from 83% to 80%) in CH<sub>4</sub> conversion was perceived. Taken into account that Ru<sub>0.035</sub>Ni<sub>0.035</sub>Mg<sub>0.93</sub>O-DR contains both Ni-rich and Ru-rich phases, the activity variation only reflects an overall contribution from heterogeneous catalytic sites containing diverse compositions and particle sizes. For Ru<sub>0.003</sub>Ni<sub>0.067</sub>Mg<sub>0.93</sub>O-DR, small activity loss (from 77% to 72%) was noticed as well. As all components are homogeneously distributed in Ru<sub>0.003</sub>Ni<sub>0.067</sub>Mg<sub>0.93</sub>O-DR, the evaluation results show that a small amount (Ru:Ni ratio of 3:67) of Ru in the bimetallic catalyst is sufficient to enhance the catalytic durability at



760 °C. In short, the directly reduced samples showed high initial activity and improved catalytic stability only for the catalyst with low Ru content, as Ru is only partially miscible with Ni. Excessively loaded catalysts show a catalytic performance out of diverse metallic sites.

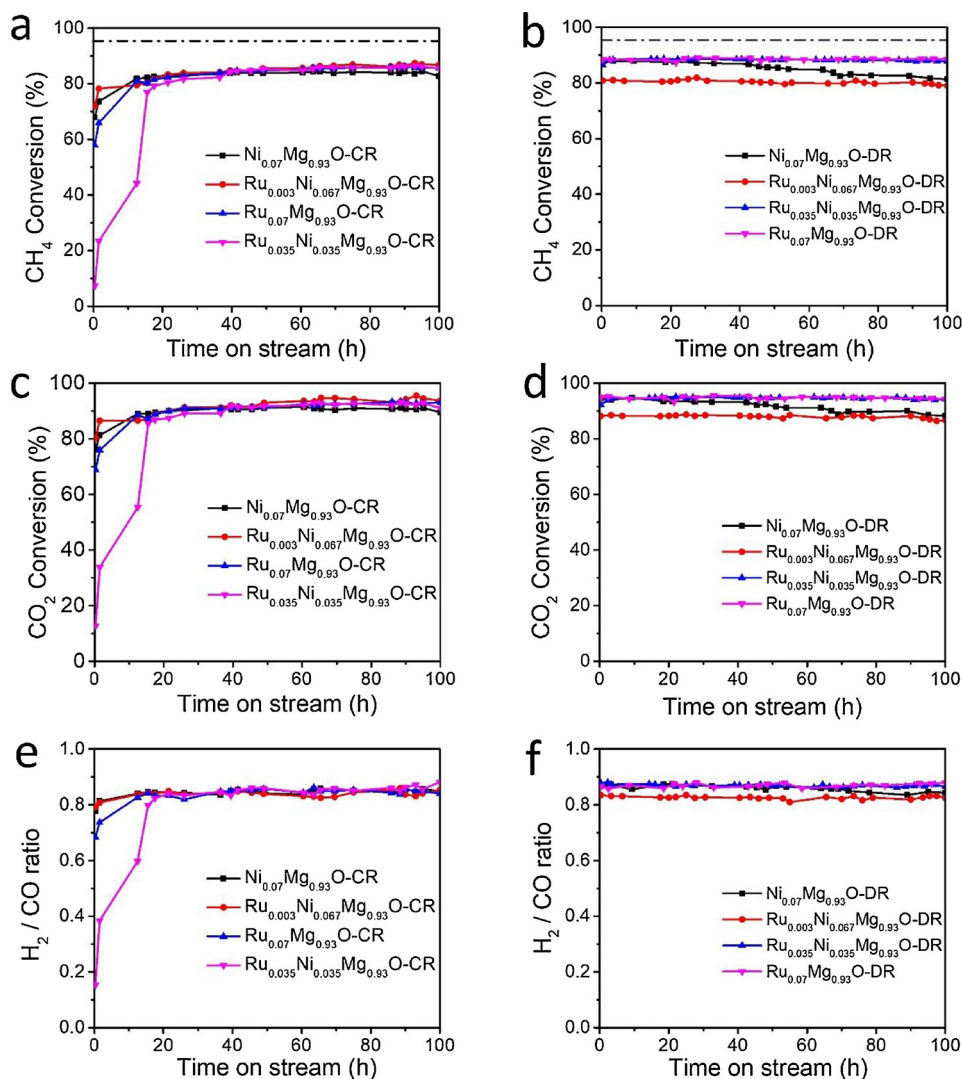
The difference in activity with respect to  $\text{Ru}_x\text{Ni}_y\text{Mg}_{1-x-y}\text{O-CR}$  samples vanished with time-on-stream, and very close activity was eventually achieved for steady state operations, recommending a stable thermodynamically equilibrated catalyst composition was reached for a given gas feed. Taken into consideration of the high operation temperature and the constant steady state contacting atmosphere composition for certain conversion levels, we conclude that although the initial activity is highly dependent on catalyst preparation history, however, the long term stability and performance is virtually unaffected by pretreatment conditions owing to the formation of ultimately thermodynamically stable structure. The  $\text{H}_2/\text{CO}$  ratios for DRM are decided by RWGS reaction (reaction 23), which is dependent on operation conditions and unaffected by catalysts used. Because RWGS reaches thermodynamic equilibria for the high reaction rate, which often out-compete methane activation that is the RDS for DRM [8]. Henceforth, identical  $\text{H}_2/\text{CO}$  ratios are often achieved at the same level of  $\text{CH}_4$  conversion, and is invariable for varied catalysts.

Fig. 5 shows the time-on-stream activities for the same samples tested at 800 °C. The initial activities of  $\text{Ru}_x\text{Ni}_y\text{Mg}_{1-x-y}\text{O-CR}$  samples at

800 °C are higher than those determined at 760 °C. Initial catalytic activities for  $\text{Ru}_{0.003}\text{Ni}_{0.067}\text{Mg}_{0.93}\text{O-CR}$ ,  $\text{Ru}_{0.035}\text{Ni}_{0.035}\text{Mg}_{0.93}\text{O-CR}$  and  $\text{Ru}_{0.07}\text{Mg}_{0.93}\text{O-CR}$  were low, but increased rapidly overtime and reached a steady state conversion before 15 h, showing that high temperature assisted recovering of activity. The  $\text{Ru}_x\text{Ni}_y\text{Mg}_{1-x-y}\text{O-DR}$  catalysts exhibited high stability and initial activity, and there is only small activity declination was observed for  $\text{Ni}_{0.07}\text{Mg}_{0.93}\text{O-DR}$ . Noteworthy, the  $\text{Ru}_{0.003}\text{Ni}_{0.067}\text{Mg}_{0.93}\text{O-DR}$  catalyst shows identical durability with that of  $\text{Ru}_{0.07}\text{Mg}_{0.93}\text{O-DR}$  during the 100 h test, and no activity loss was detected at 800 °C. This result suggests that a small amount of Ru promoter could be used to promote the long term stability of pristine Ni to a level comparable to the sole use of noble metal Ru. The high temperature stability for the two series of catalysts can be understood by taking into consideration of the theoretical predictions that increase in temperature will lead to an activation energy increase for  $\text{CH}_4$  dissociation, while a simultaneous decrease in carbon gasification activation energy, henceforth, facilitating gasification rather than carbon deposition process [9]. This rationale has been experimentally observed by several authors [23,70,72].

### 3.3. Characterizations for the spent catalysts

To shed light on the crystalline structure and composition change



**Fig. 5.** Time-on-stream stability of  $\text{Ru}_x\text{Ni}_{0.07-x}\text{Mg}_{0.93}\text{O-CR}$  (a, c) and  $\text{Ru}_x\text{Ni}_{0.07-x}\text{Mg}_{0.93}\text{O-DR}$  (b, d) catalysts at 800 °C;  $\text{CH}_4$  conversion (a, b),  $\text{CO}_2$  conversion (c, d) and the corresponding  $\text{H}_2/\text{CO}$  ratio variation (e, f). Reaction conditions: flow rates,  $\text{CH}_4 = 25 \text{ ml min}^{-1}$ ,  $\text{CO}_2 = 25 \text{ ml min}^{-1}$ ; pressure = 1.0 atm; GHSV =  $86,000 \text{ mL h}^{-1} \text{ g-cat}^{-1}$ ; catalyst weight = 0.035 g. The dashed line indicates equilibrium conversion of  $\text{CH}_4$ .

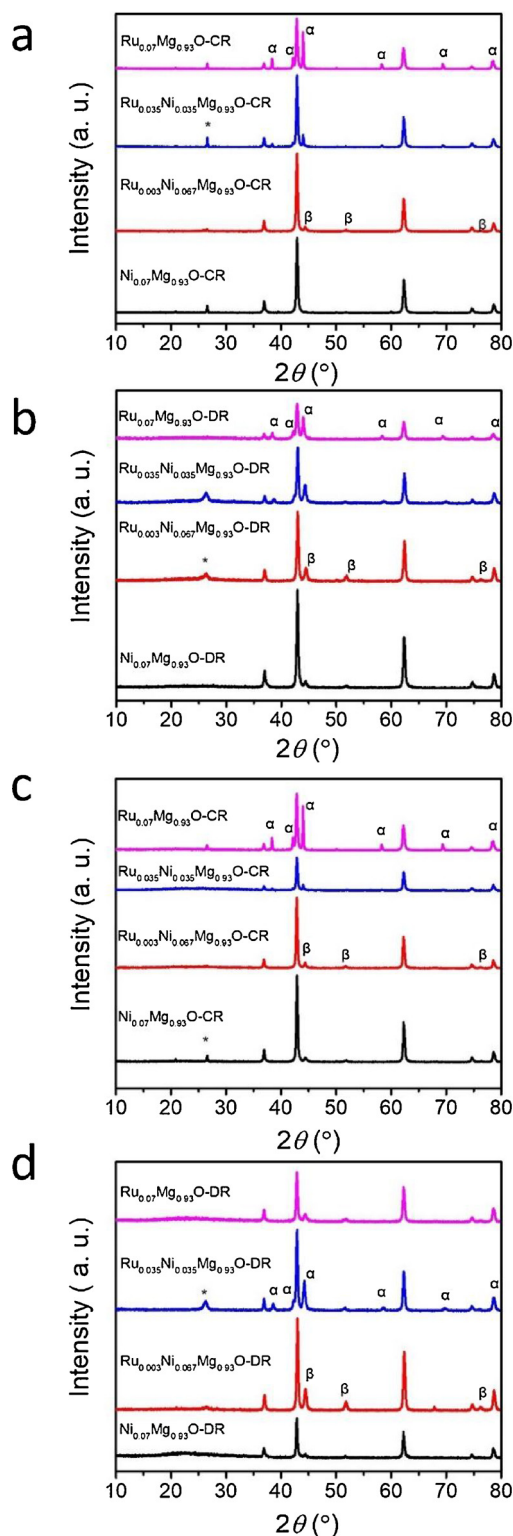


**Fig. 6.** XRD patterns for spent catalysts (a)  $\text{Ru}_x\text{Ni}_{0.07-x}\text{Mg}_{0.93}\text{O-CR}$  at 760 °C, (b)  $\text{Ru}_x\text{Ni}_{0.07-x}\text{Mg}_{0.93}\text{O-DR}$  at 760 °C, (c)  $\text{Ru}_x\text{Ni}_{0.07-x}\text{Mg}_{0.93}\text{O-CR}$  at 800 °C, and (d)  $\text{Ru}_x\text{Ni}_{0.07-x}\text{Mg}_{0.93}\text{O-DR}$  at 800 °C after 100 h time-on-stream. \* Shows diffractions out of graphite (JCPDS No. 26-1079  $2\theta = 26.6, 43.5, 46.3, 54.8$ ).  $\alpha$  indicates diffractions from Ru particles (JCPDS No. 06-0663,  $2\theta = 38.4, 42.2, 44.0, 58.3, 69.4, 78.4$ ).  $\beta$  shows diffractions out of  $\text{Ni}^0$  (JCPDS No. 04-0850,  $2\theta = 44.5, 51.8, 76.4$ ).

during the above catalytic tests, XRD patterns of the spent catalysts were collected, as presented in Fig. 6. All samples show diffraction lines from NiO-MgO solid solution, suggesting it was intact for the high

thermal stability. After tests at 760 °C,  $\text{Ni}_{0.07}\text{Mg}_{0.93}\text{O-CR}$  exhibited only a very weak  $\text{Ni}^0$  diffraction line at  $2\theta = 44.5$  (JCPDS No. 04-0850), recommending a rather small crystallite size even after 100 h test, which was attributed to the sinter-resistant property of Ni-MgO solid solution catalyst [64]. The intensity of  $\text{Ni}^0$  diffraction line increases with increasing Ru content, implying a relatively large Ru-Ni alloy size. For  $\text{Ru}_{0.035}\text{Ni}_{0.035}\text{Mg}_{0.93}\text{O-CR}$ , an additional reflection out of metallic Ru $^0$  peaks (JCPDS NO. 06-0663,  $2\theta = 38.4, 42.2, 44.0, 58.3, 69.4$  and  $78.4$ ) are observed. These results show that the catalytic activity for  $\text{Ru}_{0.035}\text{Ni}_{0.035}\text{Mg}_{0.93}\text{O-CR}$  originated from two distinct phases and the sample was heterogeneous in composition. This is in line with the Rietveld analysis of bimetallic sample Ru-Ni showing that only Ru content as low as 3 mol.% (ambient temperature) could be tolerated by the Ni-rich alloy [56] and Ru content exceeding this threshold will lead to the formation of a separate Ru-rich phase. The relatively broad peak width for Ru $^0$  compared to a sharp line for pristine  $\text{Ru}_{0.07}\text{Mg}_{0.93}\text{O-CR}$  suggests that Ru-Ni samples have smaller metallic particle size. The spent catalysts also possess graphitic carbon diffraction peaks (JCPDS No. 41-1287,  $2\theta = 26.4$ ) after the 100 h reaction at 760 °C. The spent  $\text{Ni}_{0.07}\text{Mg}_{0.93}\text{O-DR}$  and  $\text{Ru}_{0.003}\text{Ni}_{0.067}\text{Mg}_{0.93}\text{O-DR}$  showed more intensified diffraction lines from metallic  $\text{Ni}^0$  than the  $\text{Ni}_{0.07}\text{Mg}_{0.93}\text{O-CR}$  or  $\text{Ru}_{0.003}\text{Ni}_{0.067}\text{Mg}_{0.93}\text{O-CR}$  counterparts, manifesting more Ni/Ru from the precursors remained reduced during catalytic tests.

For spent catalysts after running at 800 °C for 100 h, the XRD patterns (Fig. 6c, d) are similar to these spent catalysts collected at 760 °C tests, except a few new variations. First, diffraction peaks from metallic components became more intense, showing that temperature elevation may have accelerated metallic particle growth. Second, Ru $^0$  segregated as a separate phase in spent  $\text{Ru}_{0.035}\text{Ni}_{0.035}\text{Mg}_{0.93}\text{O-CR}$  and  $\text{Ru}_{0.035}\text{Ni}_{0.035}\text{Mg}_{0.93}\text{O-DR}$  catalysts, but only  $\text{Ni}^0$  diffractions were detected for both  $\text{Ru}_{0.003}\text{Ni}_{0.067}\text{Mg}_{0.93}\text{O-CR}$  and  $\text{Ru}_{0.003}\text{Ni}_{0.067}\text{Mg}_{0.93}\text{O-DR}$ , implying that the formation of alloy is only possible for low Ru content. By comparing with the XRD patterns for fresh catalysts, one may conclude that only the catalytic performances of  $\text{Ru}_{0.003}\text{Ni}_{0.067}\text{Mg}_{0.93}\text{O-CR}$  and  $\text{Ru}_{0.003}\text{Ni}_{0.067}\text{Mg}_{0.93}\text{O-DR}$  reflect the catalytic property of a Ni rich Ru-Ni alloy, whereas  $\text{Ru}_{0.035}\text{Ni}_{0.035}\text{Mg}_{0.93}\text{O-CR}$  and  $\text{Ru}_{0.035}\text{Ni}_{0.035}\text{Mg}_{0.93}\text{O-DR}$  catalysts are heterogeneous throughout the catalytic tests. Third,  $\text{Ru}_{0.035}\text{Ni}_{0.035}\text{Mg}_{0.93}\text{O-CR}$ ,  $\text{Ru}_{0.003}\text{Ni}_{0.067}\text{Mg}_{0.93}\text{O-DR}$  and  $\text{Ru}_{0.003}\text{Ni}_{0.067}\text{Mg}_{0.93}\text{O-CR}$  did not contain graphitic carbon species that can be detected by XRD, while on spent  $\text{Ru}_{0.035}\text{Ni}_{0.035}\text{Mg}_{0.93}\text{O-DR}$  some could be identified. Overall, XRD measurements for spent catalysts corroborate the structure integrity of NiO-MgO solid solutions, and reducible Ru and Ni present in their metallic states with varied content, crystal size, and graphitic carbon contents that are highly dependent on catalyst composition, preparation or operation conditions.

In order to quantify the amount and type of carbon deposited on the catalyst surface after time-on-stream tests, TGA was conducted under successive  $\text{CO}_2$  and air atmosphere. Here, it is assumed that deposited gasifiable carbon, i.e., carbon species that are gasifiable under dry reforming reaction conditions could also be removed during TGA measurement carried out under  $\text{CO}_2$  atmosphere. The rest recalcitrant carbon species can only be eliminated by combustion in a subsequent TGA measurement undertaken in air flow. The TGA patterns are depicted in Fig. S7, and the data obtained are compiled in Table 1. In typical TGA curves, weight loss due to carbon removal took place progressively, the low temperature (300–500 °C) weight loss was assigned to C $\alpha$  [12], and the high temperature (600–700 °C) weight loss is associated with the gasification of C $\beta$ , both of which could be gasified under reforming conditions [73,74]. The  $\text{CO}_2$ -TGA actually gives a total value of the two, whereas the residues were determined by air-TGA. Over pristine  $\text{Ru}_{0.07}\text{Mg}_{0.93}\text{O-CR}$  (DR), virtually no recalcitrant carbon species (measurable by air-TGA) was detected, in line with the reported carbon-resistant performance for Ru catalysts in literatures [75]. The content of recalcitrant carbon for  $\text{Ru}_{0.07}\text{Mg}_{0.93}\text{O-CR}$ (760 °C),  $\text{Ru}_{0.07}\text{Mg}_{0.93}\text{O-CR}$  (800 °C),  $\text{Ru}_{0.07}\text{Mg}_{0.93}\text{O-DR}$ (760 °C) and  $\text{Ru}_{0.07}\text{Mg}_{0.93}\text{O-DR}$ (800 °C) was 0.20 wt.%, 0.70 wt.%, 0.7 wt.% and 1.4 wt.%, respectively. The comparison between bimetallic Ru-Ni series and that of monometallic Ni-

**Table 1**

The carbon contents are derived from TGA of the spent catalysts, gasifiable-carbon in the table represents the carbon contents (wt.%) carried out under CO<sub>2</sub> atmosphere, recalcitrant-carbon indicates the carbon contents (wt.%) obtained under air atmosphere after CO<sub>2</sub> gasification.

Catalysts	Gasifiable-carbon	Recalcitrant-carbon	Carbon ratio	Catalysts	Gasifiable-carbon	Recalcitrant-carbon	Carbon ratio
Ru <sub>0.07</sub> Mg <sub>0.93</sub> O-CR(760 °C)	2.4	0.20	12.0	Ru <sub>0.07</sub> Mg <sub>0.93</sub> O-CR(800 °C)	3.0	0.70	4.3
Ru <sub>0.035</sub> Ni <sub>0.035</sub> Mg <sub>0.93</sub> O-CR(760 °C)	3.0	0.60	5.0	Ru <sub>0.035</sub> Ni <sub>0.035</sub> Mg <sub>0.93</sub> O-CR(800 °C)	2.7	1.7	1.6
Ru <sub>0.003</sub> Ni <sub>0.067</sub> Mg <sub>0.93</sub> O-CR(760 °C)	6.0	1.6	3.8	Ru <sub>0.003</sub> Ni <sub>0.067</sub> Mg <sub>0.93</sub> O-CR(800 °C)	5.2	1.3	4.0
Ni <sub>0.07</sub> Mg <sub>0.93</sub> O-CR(760 °C)	3.8	1.4	2.7	Ni <sub>0.07</sub> Mg <sub>0.93</sub> O-CR(800 °C)	3.3	2.0	1.7
Ru <sub>0.07</sub> Mg <sub>0.93</sub> O-DR(760 °C)	2.8	0.7	4.0	Ru <sub>0.07</sub> Mg <sub>0.93</sub> O-DR(800 °C)	5.8	1.4	4.1
Ru <sub>0.035</sub> Ni <sub>0.035</sub> Mg <sub>0.93</sub> O-DR(760 °C)	21.8	2.6	7.9	Ru <sub>0.035</sub> Ni <sub>0.035</sub> Mg <sub>0.93</sub> O-DR(800 °C)	15.1	2.1	7.2
Ru <sub>0.003</sub> Ni <sub>0.067</sub> Mg <sub>0.93</sub> O-DR(760 °C)	17.7	2.5	4.7	Ru <sub>0.003</sub> Ni <sub>0.067</sub> Mg <sub>0.93</sub> O-DR(800 °C)	12.8	2.8	4.6
Ni <sub>0.07</sub> Mg <sub>0.93</sub> O-DR(760 °C)	14.4	5.1	2.8	Ni <sub>0.07</sub> Mg <sub>0.93</sub> O-DR(800 °C)	13.8	7.5	1.8

series demonstrates that addition of Ru has reduced the amount of recalcitrant carbon, i.e., Ru has altered the type of deposited carbon so that more carbon becomes gasifiable under CO<sub>2</sub> atmosphere. There is less carbon formed on spent Ru<sub>x</sub>Ni<sub>y</sub>Mg<sub>1-x-y</sub>O-CR catalysts, possibly because fewer numbers of conversions occurred as a result of their low initial activity, which makes a direct comparison disparate. The amount and type of carbon deposited over Ru<sub>0.035</sub>Ni<sub>0.035</sub>Mg<sub>0.93</sub>O-DR and Ru<sub>0.003</sub>Ni<sub>0.067</sub>Mg<sub>0.93</sub>O-DR are comparable, showing that the carbon formed is invariable towards Ru:Ni change. Another trend is that more recalcitrant carbon was formed at 760 °C than 800 °C for Ru<sub>0.035</sub>Ni<sub>0.035</sub>Mg<sub>0.93</sub>O-DR and Ru<sub>0.003</sub>Ni<sub>0.067</sub>Mg<sub>0.93</sub>O-DR catalysts, further proving that high operation temperatures are beneficial to carbon-tolerant property.

XPS for representative spent catalysts at 800 °C were collected to probe surface composition and chemical state information. Ni 2p spectra (Fig. S8) for all catalysts mainly show Ni<sup>2+</sup> 2p<sub>1/2</sub> and Ni<sup>2+</sup> 2p<sub>3/2</sub> with the chemical shift at approximately 874 eV and 855 eV, and satellite peaks at around 861 eV and 882 eV [76]. Ni-based catalysts are sensitive to exposure to the open and could be oxidized instantly in post-test handling process, and the information obtained ex-situ is therefore unimportant [77,78]. On the other hand, the C 1s spectra (Fig. S9a) gives pertinent information on the types of carbon deposited at the topmost of spent catalysts, as XPS is regarded as a surface sensitive technique. Besides the ubiquitous graphitic carbon appearing at 248.6 eV, the C 1s spectra for Ni<sub>0.07</sub>Mg<sub>0.93</sub>O-CR consists of an envelope that can be de-convoluted into the contribution from CO<sub>3</sub><sup>2-</sup>, Csp<sup>3</sup>, C–O species with chemical shifts at 288.8 eV, 287.8 eV and 285.8 eV, respectively [79–81]. With the inclusion of Ru, for spent Ru<sub>0.003</sub>Ni<sub>0.067</sub>Mg<sub>0.93</sub>O-CR and Ru<sub>0.035</sub>Ni<sub>0.035</sub>Mg<sub>0.93</sub>O-CR catalysts, the C–O shoulder peak area increased with respect to Ni<sub>0.07</sub>Mg<sub>0.93</sub>O-CR. The formation of C–O containing species is relevant to the oxyphilic nature of Ru surface, which could lead to the surface enrichment of O\* species that facilitate oxidation of carbon species [9]. No significant amount of such species was observed for pristine Ni<sub>0.10</sub>Mg<sub>0.90</sub>O catalysts in our previous investigation [64]. The increase in C–O species is also advocated by the corresponding O 1s spectra for the same samples (Fig. S9b), i.e., C–O containing species were detected on spent Ru<sub>0.035</sub>Ni<sub>0.035</sub>Mg<sub>0.93</sub>O-CR and Ru<sub>0.003</sub>Ni<sub>0.067</sub>Mg<sub>0.93</sub>O-CR catalysts, which is consistent with the aforementioned C 1s results. The same conclusion could be drawn from the comparison of XPS data for spent Ru<sub>0.003</sub>Ni<sub>0.067</sub>Mg<sub>0.93</sub>O-DR, Ru<sub>0.035</sub>Ni<sub>0.035</sub>Mg<sub>0.93</sub>O-DR series (Fig. S9b), pointing that Ru accelerates gasification of surface carbon by increasing the surface concentration of oxygenate species owing to the strong oxyphilic. The surface composition data for element percentage and carbon species over spent catalysts are tabulated in Tables S2 and S3, respectively. A higher Ru/Ni ratio (0.21 vs. 0.045) was determined via surface sensitive XPS technique that the nominal composition of the bulk, certifying Ru enrichment on the Ru<sub>0.003</sub>Ni<sub>0.067</sub>Mg<sub>0.93</sub>O-DR

catalyst surface.

TEM images of the spent catalysts for Ru<sub>0.003</sub>Ni<sub>0.067</sub>Mg<sub>0.93</sub>O-DR and Ru<sub>0.035</sub>Ni<sub>0.035</sub>Mg<sub>0.93</sub>O-DR at 800 °C are shown in Fig. S10. No conspicuous amount of whisker or encapsulating carbon species were found in the spent Ru<sub>0.003</sub>Ni<sub>0.067</sub>Mg<sub>0.93</sub>O-DR catalyst, and only occasionally trace of whisker carbon or encapsulating carbon could be identified (Fig. S10i, j), as indicated in the images by red and yellow arrows. In spent Ru<sub>0.035</sub>Ni<sub>0.035</sub>Mg<sub>0.93</sub>O-DR catalyst, however, a large amount of carbon deposition including whiskers carbon and encapsulated carbon is visible, which is in good agreement with the existence of graphitic carbon in the sample by XRD measurements (Fig. 6d). By comparing with metal particle size for fresh catalyst after H<sub>2</sub> reduction (Fig. 3j), metallic particle size has increased from 5.5 nm to 22 nm during the 100 h test for Ru<sub>0.003</sub>Ni<sub>0.067</sub>Mg<sub>0.93</sub>O-DR catalyst. In contrast, far more whisker and encapsulating carbons were found in the spent Ni<sub>0.07</sub>Mg<sub>0.93</sub>O-CR (Fig. S10a, b) catalyst, suggesting that Ru has suppressed the formation of detrimental whisker carbon. This observation shows that high Ru:Ni ratio not only leads to phase segregation, but also caused the formation of large metallic particles that loss the carbon-resistant property. No obvious carbon deposition has been observed in the TEM of Ru<sub>0.07</sub>Mg<sub>0.93</sub>O-CR catalyst (Fig. S10g, h). The TEM characterizations, in conjunction with XRD, TGA measurements, suggest that Ru<sub>0.003</sub>Ni<sub>0.067</sub>Mg<sub>0.93</sub>O-DR maps out as an outstanding catalyst showing comparable carbon-resistant performance to that of noble metal Ru<sub>0.07</sub>Mg<sub>0.93</sub>O-DR catalyst.

#### 3.4. Kinetic studies for DRM

Reaction rates were assessed for the optimized Ru<sub>0.003</sub>Ni<sub>0.067</sub>Mg<sub>0.93</sub>O-DR catalyst with a homogeneous metal distribution to find the effects of partial pressure and temperature variations on DRM rate, and comparisons were made with the two monometallic counterparts. Catalytic activity in terms of TOF was inferred from the reaction rates at 560 °C, 1 atm, as depicted in Table S4, showing that Ru as a promoter reduces the intrinsic activity of Ni catalysts. The reaction rates variation with CH<sub>4</sub> and CO<sub>2</sub> partial pressures were conducted at 760 °C at the total pressure of 1.0 atm, as illustrated in Fig. 7. Reaction rates for all three samples increase linearly with increasing CH<sub>4</sub> partial pressure, showing a first order reaction rate dependence (Fig. 7a). For monometallic Ni<sub>0.07</sub>Mg<sub>0.93</sub>O-DR and Ru<sub>0.07</sub>Mg<sub>0.93</sub>O-DR, the reaction rates run almost parallel to the abscissa with increasing CO<sub>2</sub> pressure, reflecting a zeroth reaction order with respect to CO<sub>2</sub> pressure (Fig. 7b). For Ni [8] supported on MgO and Ru [48] supported on Al<sub>2</sub>O<sub>3</sub>, Wei and Iglesia have reported first and zeroth reaction order for the two reactants, our observation is in good agreement with their proposed kinetic law.

$$r_{\text{Ni}} = k_{\text{Ni}} p_{\text{CH}_4} \quad (24)$$



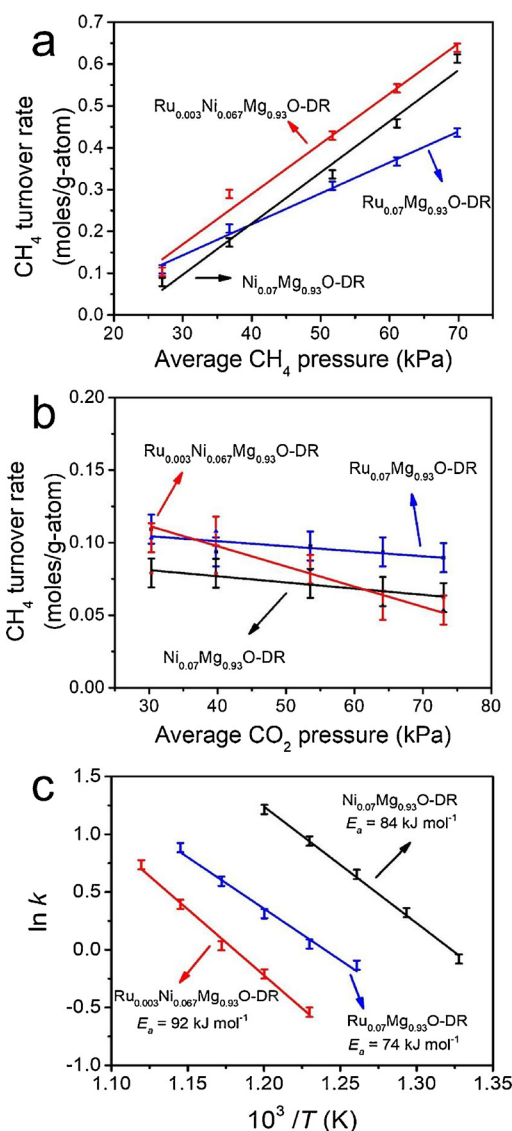


**Fig. 7.** Kinetic rate measurements of DRM as a function of (a)  $\text{CH}_4$  partial pressures and (b)  $\text{CO}_2$  partial pressures on  $\text{CH}_4$  reaction rates for  $\text{Ni}_{0.07}\text{Mg}_{0.93}\text{O-DR}$ ,  $\text{Ru}_{0.003}\text{Ni}_{0.067}\text{Mg}_{0.93}\text{O-DR}$  and  $\text{Ru}_{0.07}\text{Mg}_{0.93}\text{O-DR}$ . Test conditions: Total flow =  $93 \text{ ml min}^{-1}$ ; pressure =  $1.0 \text{ atm}$ ; catalyst weight =  $0.01 \text{ g}$ ; reaction temperature =  $760^\circ\text{C}$ , (c) Arrhenius plots for  $\text{Ni}_{0.07}\text{Mg}_{0.93}\text{O-DR}$ ,  $\text{Ru}_{0.003}\text{Ni}_{0.067}\text{Mg}_{0.93}\text{O-DR}$  and  $\text{Ru}_{0.07}\text{Mg}_{0.93}\text{O-DR}$ . Test conditions:  $\text{CH}_4 = 25 \text{ ml min}^{-1}$ ,  $\text{CO}_2 = 25 \text{ ml min}^{-1}$ ,  $\text{N}_2 = 18 \text{ ml min}^{-1}$ ; pressure =  $1.0 \text{ atm}$ ; catalyst weight =  $0.01 \text{ g}$ ; temperature range:  $500\text{--}700^\circ\text{C}$ .

$$r_{\text{Ru}} = k_{\text{Ru}} P_{\text{CH}_4} \quad (25)$$

The simple kinetic laws (Eqs. (24) and (25)) show that the surface of pristine Ni or Ru is close to clean surface as there is no denominator term that is associated with significant coverage of intermediates on metal surfaces. It also discloses that  $\text{CH}_4$  activation is the rate determining step that governs the overall reaction rate, whereas  $\text{CO}_2$  activation is kinetically unimportant. Recent reaction mechanism and micro kinetic modeling of DRM show that under ambient pressures, both  $\text{CH}_4$  and  $\text{C}^*$  oxidation could be the RDS step over pristine Ni surfaces such as flat  $\text{Ni}(111)$  or stepped  $\text{Ni}(211)$  [82,83]. For  $\text{Ru}_{0.003}\text{Ni}_{0.067}\text{Mg}_{0.93}\text{O-DR}$  catalyst, however, a small deviation from zeroth order for  $P_{\text{CO}_2}$  was disclosed. The deviation can be considered as a result of surface oxygen coverage influenced by  $P_{\text{CO}_2}$ , the similar kinetic effect has been suggested for Co-Ni alloy system, as recently reported by us [17] and confirmed by AlSabbab et al. [84]. A reaction rate for the bimetallic  $\text{Ru}_{0.003}\text{Ni}_{0.067}\text{Mg}_{0.93}\text{O-DR}$  catalyst can be

expressed as:

$$r_{\text{Ru-Ni}} = k_{\text{Ru-Ni}} P_{\text{CH}_4} \cdot \left( \frac{1}{1 + \frac{K_{\text{CO}_2} P_{\text{CO}_2}}{K_{\text{CO}} P_{\text{CO}}}} \right) = k_{\text{Ru-Ni}} P_{\text{CH}_4} \cdot \left( \frac{1}{1 + K' P_{\text{CO}_2}} \right) \quad (26)$$

Whereby  $K'$  is the corresponding dissociative adsorption constant for  $\text{CO}_2$ ,  $k_{\text{Ru-Ni}}$  is the reaction rate constant for  $\text{Ru}_{0.003}\text{Ni}_{0.067}\text{Mg}_{0.93}\text{O-DR}$  catalyst,  $K_{\text{CO}_2}$  and  $K_{\text{CO}}$  are the thermodynamic equilibrium constant for reaction 27 and 28, respectively,  $P_{\text{CO}}$ ,  $P_{\text{CH}_4}$  and  $P_{\text{CO}_2}$  are the partial pressures of  $\text{CO}$ ,  $\text{CH}_4$  and  $\text{CO}_2$ , respectively.  $\text{CO}_2$  dissociation is a kinetically fast step that equilibrates with surface  $\text{O}^*$  and  $\text{CO}^*$ , and the later desorbs instantly and leaves behind  $\text{O}^*$  as the most abundant surface species. As  $\text{O}^*$  is the most abundant surface intermediate (MASI) that compete with  $\text{CH}_4$  dissociation for active sites and  $P_{\text{CO}}$  is regarded invariable at low conversion levels and high space velocity, under such conditions negligibly contribution from re-adsorption can be guaranteed, and the measured reaction rate declines with increasing  $P_{\text{CO}_2}$ . Indeed,  $\text{CO}$  adsorption at reforming conditions is less likely for the high reaction temperatures.



A  $K'$  value of  $0.027 \text{ kPa}^{-1}$  can be inferred from this simple model.

Activation energies on  $\text{Ni}_{0.07}\text{Mg}_{0.93}\text{O-DR}$ ,  $\text{Ru}_{0.07}\text{Mg}_{0.93}\text{O-DR}$  and  $\text{Ru}_{0.003}\text{Ni}_{0.067}\text{Mg}_{0.93}\text{O-DR}$  were determined from Arrhenius plot (Fig. 7c) to be  $84$ ,  $74$  and  $92 \text{ kJ mol}^{-1}$ , respectively. Activation energies reported for  $\text{Ni/MgO}$  and  $\text{Ru/Al}_2\text{O}_3$  by Wei and Iglesia [8,48] are  $105$  and  $96 \text{ kJ mol}^{-1}$ , respectively. We ascribe the difference to the effect of  $\text{NiMgO}(111)$  solid solution support, and the Tasker III type facets which can impart a stronger metal-support interaction that imposes a support effect [62]. The activation energy for the bimetallic  $\text{Ru}_{0.003}\text{Ni}_{0.067}\text{Mg}_{0.93}\text{O-DR}$  catalyst is higher than the two monometallic catalysts, very possibly because of the formation of a Ru-rich interface over Ru-Ni alloy particle under reforming conditions. This inference is further advocated by the following facts. First, on Ni overlayer modified  $\text{Ru}(0001)$  surface, an increase in activity for methane activation by a factor of  $20\text{--}30$  with respect to Ni has been observed by Egeberg and Chorkendorff under Ultrahigh Vacuum (UHV) chamber [85], showing that Ni-rich interface would lower the activation barrier associated with  $\text{CH}_4$  dissociation. Their results are contrary to our observations. Second, the presence  $\text{O}^*$  on Ru-Ni surface can incur a pseudomorphic overlayer of Ru, whereby surface Ru occupies lattice positions of the Ni fcc substrate, has formed under reaction conditions. As Ru has larger atomic radius ( $149$  vs.  $178 \text{ pm}$ ), the alloying of Ru with Ni (adopting the same fcc structure as for metallic Ni, that can be inferred from XRD pattern) would compress the distance between adjacent atoms with respect to pristine Ru, leading to a concurrent increase in coordination number and down shift of  $d$ -band center, according to the simple model of surface reactivity of transition and noble metals [86]. As  $d$ -band is shifted further below the Fermi level, surface adsorption energy of carbon atoms, or surface ability to activate  $\text{CH}_4$  will become less negative accordingly [86]. Consequently, an increased activation barrier has been observed experimentally.

Ru influence can be summarized to be: 1. Increasing kinetic barrier for  $\text{CH}_4$  dissociation which is the common limiting step for both DRM and carbon deposition [8], and henceforth slows down the carbon deposition rate. 2. Enhancing  $\text{O}^*$  surface coverage in Ru-Ni alloy surface that promotes gasification. Surface coverage of  $\text{O}^*$  or  $\text{OH}^*$  species will kinetically promote the rate of gasification [9]. The surface coverage increase of  $\text{O}^*$  or  $\text{OH}^*$  species may have also altered the surface composition of Ru-Ni, as a higher Ru/Ni ratio and more C–O species were determined from the XPS measurements for spent catalysts (Fig. S9, Table S2).

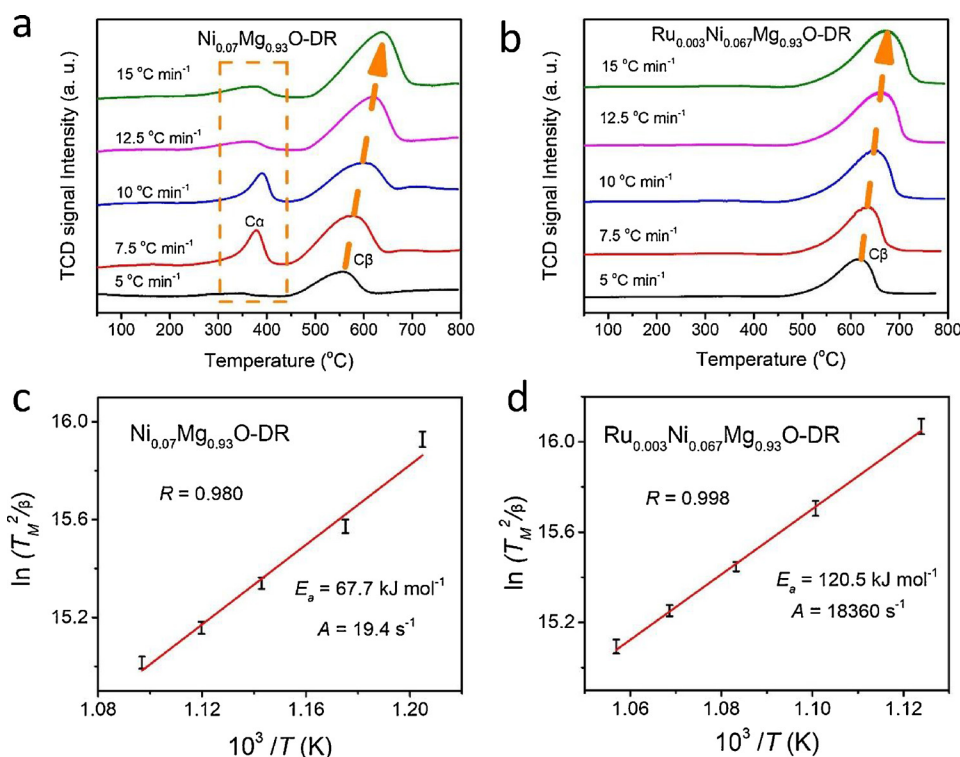


**Fig. 8.** CO<sub>2</sub>-TPO patterns for Ni<sub>0.07</sub>Mg<sub>0.93</sub>O-DR (a) and Ru<sub>0.003</sub>Ni<sub>0.067</sub>Mg<sub>0.93</sub>O-DR (b) with manipulated heating rates of 5, 7.5, 10, 12.5, 15 °C min<sup>-1</sup> from 30 °C to 800 °C in CO<sub>2</sub> (100 vol.%) flow (30 ml min<sup>-1</sup>). The corresponding fitting data from (a) and (b) with Eq. (21) are shown in (c) and (d), respectively.

### 3.5. Carbon gasification kinetics of spent catalysts

To determine carbon gasification kinetics, we proposed a modified CO<sub>2</sub>-TPO measurement to obtain kinetic data from carbon gasification on spent catalysts by extrapolating Wigner–Polanyi equation, as there was no established method. The acquired CO<sub>2</sub>-TPO patterns under controlled heating rates are depicted in Fig. 8(a, b), and the corresponding plots of  $\ln(T_M^{2/\beta})$  vs. reciprocal temperature  $1/T$  are presented in Fig. 8(c, d). The temperatures of maximum rates ( $T_M$ ) for surface carbon oxidation determined by TCD signal, were found to increase with increasing heating rates, vary from 555 to 636 °C and 617 to 674 °C for the spent Ni<sub>0.07</sub>Mg<sub>0.93</sub>O-DR and Ru<sub>0.003</sub>Ni<sub>0.067</sub>Mg<sub>0.93</sub>O-DR catalysts, respectively. The low catalytic activity of Ru<sub>0.003</sub>Ni<sub>0.067</sub>Mg<sub>0.93</sub>O-DR catalyst is ascribed to the oxidation of Ru and Ru-Ni surface by CO<sub>2</sub> that has been activated by the basic support of Ni-MgO solid solution.

For monometallic Ni<sub>0.07</sub>Mg<sub>0.93</sub>O-DR catalyst, there are two gasification peaks that can be discerned from the CO<sub>2</sub>-TPO profile (Fig. 8a), a low temperature gasification of highly reactive Cα species appearing at 330–420 °C that is nearly independent of heating rates, and a high temperature gasification peak that can be attributed to the gasification of less reactive Cβ [13]. Both surface carbon species can be gasified by CO<sub>2</sub> into CO (reaction 13), but at distinguishable temperatures [73,74]. As the spent catalysts were collected from the same test, the variation of Cα amount is presumably ascribed to the mounting position of sampled spent catalysts, as carbon amount was often found to decrease from inlet to outlet on Ni-based catalysts [72]. The low temperature gasification of Cα implies that this type of surface carbon is highly reactive upon contacting with CO<sub>2</sub>, showing invariable  $T_M$  with increasing heating ramp, hence, the kinetic model used here is not applicable for the deduction of kinetic data for Cα gasification. It is also possible that Cα gasification is kinetically fast that the process requires little driven force. On Ru<sub>0.003</sub>Ni<sub>0.067</sub>Mg<sub>0.93</sub>O-DR catalyst, only Cβ can be identified, showing that Cα was completely gasified under DRM test. Unlike Cα,  $T_M$  for Cβ shifts to high temperatures with increasing heating rates. By fitting the  $T_M$  variations with heating rates using Eq. (21), a good

linearity gives Cβ gasification activation energy of 67.7 kJ mol<sup>-1</sup> and 120.5 kJ mol<sup>-1</sup>, for Ni<sub>0.07</sub>Mg<sub>0.93</sub>O-DR and Ru<sub>0.003</sub>Ni<sub>0.067</sub>Mg<sub>0.93</sub>O-DR catalysts, respectively. The comparison demonstrates that Ru gives rise to a disfavored increase in activation energy for Cβ gasification. Meanwhile, the pre-exponential factor  $A$  were found to be 19.4 s<sup>-1</sup> and 18,360 s<sup>-1</sup> for Ni<sub>0.07</sub>Mg<sub>0.93</sub>O-DR and Ru<sub>0.003</sub>Ni<sub>0.067</sub>Mg<sub>0.93</sub>O-DR catalysts, respectively. The kinetic data are tabulated in Table 2, and a temperature dependence reaction rate constants variation for both catalysts are shown in Fig. S11 in the Supporting information. The overall gasification rate constant  $k$  for Ru<sub>0.003</sub>Ni<sub>0.067</sub>Mg<sub>0.93</sub>O-DR is larger than Ni<sub>0.07</sub>Mg<sub>0.93</sub>O-DR above 655 °C (Fig. S11), and the number was 0.0098 s<sup>-1</sup> and 0.025 s<sup>-1</sup> for Ni<sub>0.07</sub>Mg<sub>0.93</sub>O-DR and Ru<sub>0.003</sub>Ni<sub>0.067</sub>Mg<sub>0.93</sub>O-DR catalysts at 800 °C (Table S5), respectively. As the Pre-exponential factor for Ru<sub>0.003</sub>Ni<sub>0.067</sub>Mg<sub>0.93</sub>O-DR is 3 orders of magnitude larger than for Ni<sub>0.07</sub>Mg<sub>0.93</sub>O-DR, which is sufficient to offset the disfavored high activation barrier. The difference between the pre-exponential factors is due to the existence of the compensation effect, resulting possibly from the fact that the activation energy contains coverage-dependent, second-order terms, which are usually ignored [87].

In order to obtain gasification order with respect to  $P_{\text{CO}_2}$ , another series of CO<sub>2</sub>-TPO profiles were obtained by correlating the maximum gasification peak with  $P_{\text{CO}_2}$  variation, as shown in Fig. 9(a, b). The fitting data by plotting  $\ln(T_M^{2/\beta}) - \frac{E_a}{RT_M}$  as a function of  $\ln P_{\text{CO}_2}$  using Eq.

**Table 2**

Kinetic parameters derived from the carbon gasification kinetic measurements of spent catalysts, the temperature dependence of reaction constant  $k$  is shown in Fig. S11 in the Supporting information.

Catalysts	$E_a^a$ kJ mol <sup>-1</sup>	$A^a$ s <sup>-1</sup>	$n^b$	$A^b$ s <sup>-1</sup>
Ni <sub>0.07</sub> Mg <sub>0.93</sub> O-DR	67.7	19.4	0.50	21.0
Ru <sub>0.003</sub> Ni <sub>0.067</sub> Mg <sub>0.93</sub> O-DR	120.5	18,360	0.62	19,480

<sup>a</sup> Pre-exponential factor derived from Eq. (21).

<sup>b</sup> Pre-exponential factor calculated from Eq. (22).

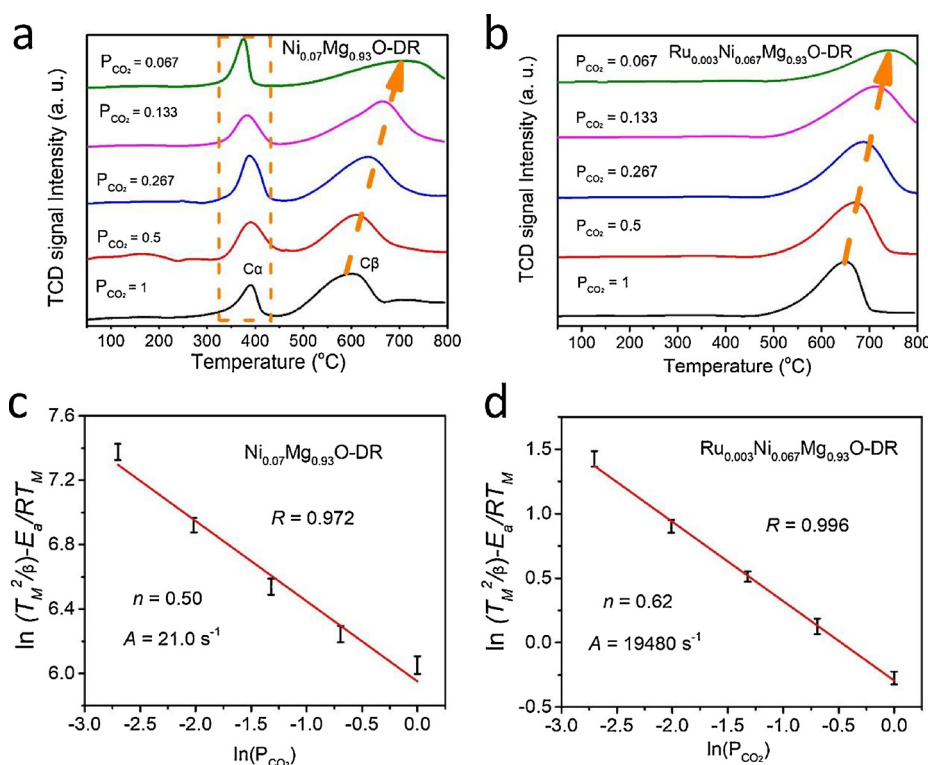


**Fig. 9.** CO<sub>2</sub>-TPO patterns for Ni<sub>0.07</sub>Mg<sub>0.93</sub>O-DR (a) and Ru<sub>0.003</sub>Ni<sub>0.067</sub>Mg<sub>0.93</sub>O-DR (b) with varying partial pressure of CO<sub>2</sub> (100, 50, 26.7, 13.3, 6.7 vol. %)/He flow (The total flow was 30 ml min<sup>-1</sup>) at the same ramp of 10 °C min<sup>-1</sup> by heating from 30 °C to 800 °C. The corresponding fitting data from (a) and (b) with Eq. (22) are shown in (c) and (d), respectively.

(22) are illustrated in Fig. 9(c, d) for both spent catalysts, approximate overall reaction orders of 0.50 and 0.62 can be inferred from the linearity relationship, and a pre-exponential factor of 21.0 s<sup>-1</sup> and 19,480 s<sup>-1</sup> for  $A$  can be calculated for Ni<sub>0.07</sub>Mg<sub>0.93</sub>O-DR and Ru<sub>0.003</sub>Ni<sub>0.067</sub>Mg<sub>0.93</sub>O-DR catalysts, respectively. Pre-exponential factor values derived from both Eqs. (21) and (22) are comparable, indicating the deduction is a reasonably good estimation. It is noteworthy that integer reaction orders with respect to pressure change for gasification kinetic law is based on Langmuir-Hinshelwood law, which applies to surface species that are randomly distributed in the absence of lateral interactions [88]. When carbon islands or polymeric carbon species (such as Cβ) reside on Ni surfaces, however, this kinetic law may no longer hold because gasification could only take place on the periphery of carbon islands or polymeric species, and a smaller than first reaction order may be expected. A relatively large reaction order for Ru<sub>0.003</sub>Ni<sub>0.067</sub>Mg<sub>0.93</sub>O-DR (0.62) with respect to Ni<sub>0.07</sub>Mg<sub>0.93</sub>O-DR (0.50) might suggest smaller carbon islands formation on alloy surface than on Ni surface. Small carbon islands are more close to random distribution of surface carbon on the metal surface which shows the first order. The formation of large carbon islands on Ni surface would reduce the gasification rate effectively, owing to a reduced contacting circumference whereby surface O\* meets surface C\* and gasification takes place.

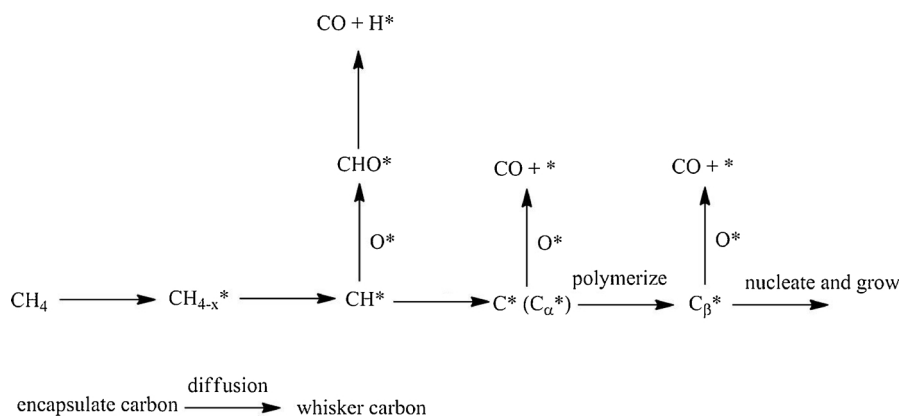
#### 4. General discussion

Ru-Ni catalyst undergoes complicated structure and composition changes during commonly used calcination and reduction procedures, owing to the oxidation and reduction caused phase segregations, and these changes are responsible for the heterogeneity of catalysts. For the same reason, Ru-Ni-MgO catalysts generated from the same precursor Ru<sub>x</sub>Ni<sub>y</sub>Mg<sub>1-x-y</sub>(OH)(OCH<sub>3</sub>) differ in composition and structure. In the calcination process, RuO<sub>2</sub> could easily segregate at high loadings as it does not form stable mixed oxides with NiO-MgO solid solutions. In addition, H<sub>2</sub> reduction pretreatment easily lead to the formation of distinct Ru<sup>0</sup> and Ni<sup>0</sup> particles as the two metals are essentially immiscible. It is therefore difficult to establish a reliable structure-

catalysis relationship as diverse composition and structure can co-exist in the same catalysts. This heterogeneity may explain why the reported catalytic behaviors are not always consistent in the open literatures [50,56,71]. As shown in this study, the pretreatment conditions can severely impact catalyst structure and homogeneity, which eventually brings about the observed catalytic property difference. The catalytic performance of Ru<sub>0.035</sub>Ni<sub>0.035</sub>Mg<sub>0.93</sub>O(-DR, or -CR) with the equal amount of Ru and Ni actually consists of two contributions from distinct Ru- rich and Ni- rich phases. Even for Ru<sub>0.003</sub>Ni<sub>0.067</sub>Mg<sub>0.93</sub>O-DR that is homogeneous in composition, but a low initial activity has been observed. The attempted direct reduction of precursor produced a Ru<sub>0.003</sub>Ni<sub>0.067</sub>Mg<sub>0.93</sub>O-DR sample with homogeneous composition and microscopic structure, thus permitting the establishment of a reliable structure-catalysis relationship. This sample has a small metal particle size and narrow size distribution with respect to monometallic Ni<sub>0.07</sub>Mg<sub>0.93</sub>O catalyst, and the activity is stable up to 100 h during the time-on-stream test at 800 °C, despite that metal growth was also identified.

To illustrate the influence of Ru on carbon deposition over the Ni-based catalyst, kinetic studies were carried out on the Ru<sub>0.003</sub>Ni<sub>0.067</sub>Mg<sub>0.93</sub>O-DR with proven homogeneity and carbon-resistant property. It is useful to take into account the carbon formation and gasification mechanism to understand the effect of Ru, as outlined in Scheme 1. At temperatures above 557 °C, the major reaction responsible for carbon deposition is CH<sub>4</sub> decomposition, CH<sub>4</sub> undergoes sequential deprotonation in the reaction pathway to CH<sub>3</sub>\*, CH<sub>2</sub>\*, CH\* or atomically adsorbed C\*(Cα) or polymeric Cβ, and co-produce H\*, H\* combines each other to desorb quickly as H<sub>2</sub> (Scheme 1). Nucleation and growth of surface carbon can produce encapsulating carbon, or whisker carbon when diffusion of carbon atom is involved. In this sequence, only encapsulating carbon may cause deactivation as it reduces the number of active sites by blocking. Gasification of these carbon-containing intermediates by surface O\* released by CO<sub>2</sub> dissociation produces CO. The gasification rate could also become a RDS when carbon deposition overrates gasification, and Cα or Cβ is accumulated on catalyst surfaces. On pristine Ni catalyst, the surface coverage of intermediates such as CH<sub>3</sub>\*, CH<sub>2</sub>\*, CH\* is negligibly low and





**Scheme 1.** Carbon deposition from methane fragmentation and its gasification mechanism in reforming reaction.

gasification mainly occurs through  $\text{C}_\alpha$  or  $\text{C}_\beta$  surface oxidation, as reflected by the reaction mechanism and theoretical predictions [7,11–13,82]. Virtually, no  $\text{CH}_3^*$ ,  $\text{CH}_2^*$ ,  $\text{CH}^*$  intermediates have ever been identified under reforming reaction conditions (even by in situ techniques) on Ni surface, and only diverse types of carbon species are often experimentally observed, suggesting that they can be readily converted to carbon species as a result of fast kinetics originating from progressively lowered activation barriers for their deprotonation. The observation of carbon species also reflects that their oxidation to CO could also be a slow step. From kinetic studies, it is convinced that  $\text{CH}_4$  dissociation is the RDS for the overall reaction, which is also the step that is controlling carbon deposition. Gasification is mainly controlled by the surface ability to oxidize various carbon species. For pristine Ni catalyst, more  $\text{C}_\beta$  and whisker carbon) are found on spent catalysts, which can be attributed to fast carbon deposition and slow gasification. With the introduction of Ru, on the one hand, Ru-Ni alloy slows down carbon formation rate by elevating the activation energy for  $\text{CH}_4$  dissociation, which is the RDS for both reforming and  $\text{CH}_4$  decomposition reactions. On the other hand, Ru-Ni alloy also exhibits an enhanced gasification rate, as 3 orders of magnitude increase in the pre-exponential factor was identified, which counteracts the disfavored high activation barrier for carbon oxidation with  $\text{CO}_2$ . The simultaneous increase in activation energies for both carbon formation and gasification is plausible, as  $\text{CH}_4$  activation is found to scale with  $\text{C}^*$  adsorption energy, while oxidation capability is associated with  $\text{O}^*$  adsorption also by a scaling relationship [89]. Ru-Ni alloy favors dissociative  $\text{CO}_2$  adsorption, as evidenced by a perceivable  $\text{O}^*$  coverage by XPS measurements on spent catalysts, which can also be envisaged by the kinetic law and oxyphilic nature of Ru [9]. Increasing of surface  $\text{O}^*$  concentration will lead to a faster oxidation of carbon species as well [7], which may counteract the slow carbon oxidation resulting from high activation energy as well. Furthermore, formation of Ru-Ni alloy also gives rise to a change of the distance between two hollow sites on which C atoms are adsorbed, which disfavors carbon nucleation towards whisker carbon [11], since distance between these sites on pristine Ni (for instance 0.251 nm for Ni(111)) surface is rather close to C–C bond length (0.246 nm) and favors polymerization. In short, Ru brings about beneficiary slowed carbon deposition rate, surface oxygen coverage and possibly small ensemble size, and simultaneously accelerate carbon gasification particularly at high temperatures.

Regarding the effect of Ru on surface  $\text{C}^*$  oxidation pathway, it was theoretically postulated by Jiao et al. [90,91] that  $\text{CH}^*$  combination with surface  $\text{O}^*$  (in some other models,  $\text{OH}^*$  was also considered as an oxidant [92]) to intermediate  $\text{HCO}^*$  and its decomposition to  $\text{CO}^*$  and  $\text{H}^*$ , rather than  $\text{C}^*$  direct oxidation with  $\text{O}^*$  to  $\text{CO}^*$ , is more kinetically favorable for the low energetic barrier on Ni surfaces. However, given the low adsorption energy of  $\text{CH}^*$  and consequently its low surface coverage over pristine Ni surface,  $\text{C}^*$  reacting with  $\text{O}^*$  is often regarded

as the main pathway for surface carbon oxidation [9]. Alternatively, for Ru-Ni alloy surface, the most abundant reaction intermediate becomes  $\text{O}^*$ , deprotonated intermediates such as  $\text{CH}_3^*$ ,  $\text{CH}_2^*$  or  $\text{CH}^*$  can be facily oxidized by the available surface  $\text{O}^*$  before becoming  $\text{C}^*$ , thus opening new gasification reaction channels.

Carbon gasification kinetic studies by  $\text{CO}_2$  on spent catalysts show that our proposed method is applicable to the generation of kinetic data. The effect of Ru on temperature-dependent gasification kinetics is disclosed and Ru is able to accelerate  $\text{CO}_2$  gasification of surface carbon at high temperatures. The effect is mainly an increase in the pre-exponential factor. Such a speculation is advocated by the comparison of durability between 760 and 800 °C, showing that more stable running and less carbon deposition can be achieved at 800 °C. In addition, the finding that gasification is advantageous in the  $\text{CO}_2$  rich atmosphere as the corresponding rate increases with increasing  $\text{CO}_2$  partial pressure may be important for carbon-resistant process design. For instance, in the  $\text{CO}_2$  rich atmosphere like in the upstream of the catalyst bed, the  $\text{O}^*$  coverage is expected to be high and the gasification rates on metal surface are anticipated to be high, resultantly, the carbon-resistant function is maximized. In the  $\text{CO}_2$  lean atmosphere, such as near the exit of the catalyst bed, where most  $\text{CO}_2$  has been consumed, the gasification rate may drop and the Ru-Ni catalyst is foreseen to partially lose its carbon-resistant property. Such characteristics imply that the Ru-Ni catalyst will perform better with a surplus of  $\text{CO}_2$  in the feed. This atmosphere-dependence of carbon-resistant performance also suggests that distinct catalyst should be mounted in an appropriate position of a catalyst bed, so as to match the varied performance requirements.

## 5. Conclusions

A solvothermal synthesis to prepare  $\text{Ru}_x\text{Ni}_{0.07-x}\text{Mg}_{0.93}(\text{OH})(\text{OCH}_3)$  precursor possessing controlled surface orientation normal to (001) facets of the  $R\bar{3}m$  structure and homogeneously distributed Ru, Ni, Mg is used to prepare Ru-Ni-MgO(111) catalysts. Phase segregation could easily happen in the preparation stages such as calcination and reduction pretreatment, causing heterogeneity of catalysts, varied catalytic properties, as well as diverse carbon-resistant properties. Only for a directly reduced catalyst with small Ru loading can homogeneity of catalyst be achieved, which exhibits improved 100 h durability at 800 °C. The role of Ru is disclosed to slow down  $\text{CH}_4$  dissociation that is the rate determining step for carbon deposition rate, accelerate surface carbon oxidation by  $\text{CO}_2$ , as well as enhancing surface oxygen coverage. A pseudomorphic overlayer of Ru rich surface formed under reaction conditions is proposed grounded on kinetic measurements, as a larger atom such as Ru on top of a metal with the smaller radius gives rise to a downwards shift of  $d$  states, and consequently decrease of carbon affinity and the increase of  $\text{CH}_4$  dissociation barrier. It is instructive to conclude that the catalytic performance for Ru-Ni alloy catalyst in DRM

is primarily influenced by the formation of Ru rich pseudomorphic overlayer in response to the contacting atmosphere, due to the oxygen affinity of Ru and the difference in atomic radius and their immiscible nature. A high operation temperature as well as the high partial pressure of CO<sub>2</sub> in the atmosphere is expected to favor carbon gasification, according to the derived kinetic law for carbon gasification.

## Acknowledgements

XZ is sponsored by the National Natural Science Foundation of China (U1162112). KZ is grateful for the financial support from National Natural Science Foundation of China (21576082), Fundamental Research Funds for the Central Universities (No. WB 222201718003) and Financial Support from Sinopec Group (Contract No. 415063).

## Appendix A. Supplementary data

Supplementary material related to this article can be found, in the online version, at doi:<https://doi.org/10.1016/j.apcatb.2018.03.103>.

## References

- [1] P.M. Mortensen, I. Dybkjae, *Appl. Catal. A: Gen.* 495 (2015) 141–151.
- [2] W.-M. Chen, Y.-J. Ding, D.-H. Jiang, T. Wang, H.-Y. Luo, *Catal. Commun.* 7 (2006) 559–562.
- [3] F. Yagi, R. Kanai, S. Wakamatsu, R. Kajiyama, Y. Suehiro, M. Shimura, *Catal. Today* 104 (2005) 2–6.
- [4] J.R. Rostrup-Nielsen, S. Jens, J.K. Nørskov, *Adv. Catal.* 47 (2002) 65–139.
- [5] G.A. Olah, A. Goepfert, M. Czaun, G.K.S. Prakash, *J. Am. Chem. Soc.* 135 (2012) 648–650.
- [6] D. Pakhare, J. Spivey, *Chem. Soc. Rev.* 43 (2014) 7813–7837.
- [7] H.S. Bengaard, J.K. Nørskov, J. Sehested, B.S. Clausen, L.P. Nielsen, A.M. Molenbroek, J.R. Rostrup-Nielsen, *J. Catal.* 209 (2002) 365–384.
- [8] J. Wei, E. Iglesia, *J. Catal.* 224 (2004) 370–383.
- [9] G. Jones, J.G. Jakobsen, S.S. Shim, J. Kleis, M.P. Andersson, J. Rossmel, F. Abild-Pedersen, T. Bligaard, S. Helveg, B. Hinnemann, J.R. Rostrup-Nielsen, I. Chorkendorff, J. Sehested, J.K. Nørskov, *J. Catal.* 259 (2008) 147–160.
- [10] M.-S. Fan, A.Z. Abdullah, S. Bhatia, *ChemCatChem* 1 (2009) 192–208.
- [11] S. Helveg, C. López-Cartes, J. Sehested, P. Hansen, B.S. Clausen, J.R. Rostrup-Nielsen, F. Abild-Pedersen, J.K. Nørskov, *Nature* 427 (2004) 426–429.
- [12] J.G. McCarty, H. Wise, *J. Catal.* 57 (1977) 406–416.
- [13] D.L. Trimm, *Catal. Today* 49 (1999) 3–10.
- [14] I. Luisetto, S. Tuti, C. Battocchio, S. Lo Mastro, A. Sodo, *Appl. Catal. A: Gen.* 500 (2015) 12–22.
- [15] K. Tomishige, O. Yamazaki, Y. Chen, K. Yokoyama, X. Li, K. Fujimoto, *Catal. Today* 45 (1998) 35–39.
- [16] Y.H. Hu, E. Ruckenstein, *Cat. Rev.—Sci. Eng.* 44 (2002) 423–453.
- [17] X. Fan, Z. Liu, Y.-A. Zhu, G. Tong, J. Zhang, C. Engelbrekt, J. Ulstrup, K. Zhu, X. Zhou, *J. Catal.* 330 (2015) 106–119.
- [18] J.-H. Kim, D.J. Suh, T.-J. Park, K.-L. Kim, *Appl. Catal. A: Gen.* 197 (2000) 191–200.
- [19] T.H. Gardner, J.J. Spivey, E.L. Kugler, D. Pakhare, *Appl. Catal. A: Gen.* 455 (2013) 129–136.
- [20] S. Gaur, D.J. Haynes, J.J. Spivey, *Appl. Catal. A: Gen.* 403 (2011) 142–151.
- [21] J.R. Rostrup-Nielsen, *Chem. Eng. Sci.* 50 (1995) 4061–4071.
- [22] D. Baudouin, J.-P. Candy, U. Rodemerck, F. Krumeich, L. Veyre, P.B. Webb, C. Thieuleux, C. Copéret, *Catal. Today* 235 (2014) 237–244.
- [23] E. Nikolla, J. Schwank, S. Linic, *J. Catal.* 263 (2009) 220–227.
- [24] T. Stroud, T. Smith, E.L. Saché, J.L. Santos, M.A. Centeno, H. Arellano-Garcia, J.A. Odriozola, T.R. Reina, *Appl. Catal. B: Environ.* 224 (2018) 125–135.
- [25] M. Yu, Y.-A. Zhu, Y. Lu, G. Tong, K. Zhu, X. Zhou, *Appl. Catal. B: Environ.* 165 (2015) 43–56.
- [26] N.V. Parizotto, K.O. Rocha, S. Damyanova, F.B. Passos, D. Zanchet, C.M.P. Marques, J.M.C. Bueno, *Appl. Catal. A: Gen.* 330 (2007) 12–22.
- [27] R.T. Vang, K. Honkala, S. Dahl, E.K. Vestergaard, J. Schnadt, E. Laegsgaard, B.S. Clausen, J.K. Nørskov, F. Besenbacher, *Nat. Mater.* 4 (2005) 160–162.
- [28] A. Horváth, L. Guzzi, A. Kocsanya, G. Sáfrán, V. La Parola, L.F. Liotta, G. Pantaleo, A.M. Venezia, *Appl. Catal. A: Gen.* 468 (2013) 250–259.
- [29] F. Besenbacher, I. Chorkendorff, B.S. Clausen, B. Hammer, A.M. Molenbroek, J.K. Nørskov, I. Stensgaard, *Science* 279 (1998) 1913–1915.
- [30] M.S. Aw, M. Zorko, P. Djinić, A. Pintar, *Appl. Catal. B: Environ.* 164 (2015) 100–112.
- [31] H. Arbag, S. Yasyerli, N. Yasyerli, G. Dogu, T. Dogu, *Appl. Catal. B: Environ.* 198 (2016) 254–265.
- [32] L. Yang, Y. Choi, W. Qin, H. Chen, K. Blinn, M. Liu, P. Liu, J. Bai, T.A. Tyson, M. Liu, *Nat. Commun.* 2 (2011) 357–365.
- [33] C. Wang, N. Sun, M. Kang, X. Wen, N. Zhao, F. Xiao, W. Wei, T. Zhao, Y. Sun, *Catal. Sci. Technol.* 3 (2013) 2435–2443.
- [34] K. Jabbour, P. Massiani, A. Davidson, S. Casale, N.E. Hassan, *Appl. Catal. B: Environ.* 201 (2017) 527–542.
- [35] S.M. Kim, P.M. Abdala, T. Margossian, D. Hosseini, L. Foppa, A. Armutulu, B.W. Van, A. Comasvives, C. Copéret, C. Mueller, *J. Am. Chem. Soc.* 139 (2017) 1937–1949.
- [36] S.A. Theofanidis, V.V. Galvita, H. Poelman, G.B. Marin, *ACS Catal.* 5 (2015) 3028–3039.
- [37] J. Ashok, S. Kawi, *ACS Catal.* 4 (2014) 289–301.
- [38] S.A. Theofanidis, R. Batchu, V.V. Galvita, H. Poelman, G.B. Marin, *Appl. Catal. B: Environ.* 185 (2016) 42–55.
- [39] V.A. Tsipouriari, X.E. Verykios, *Catal. Today* 64 (2001) 83–90.
- [40] X. Li, D. Li, H. Tian, L. Zeng, Z.J. Zhao, J. Gong, *Appl. Catal. B: Environ.* 202 (2017) 683–694.
- [41] A.S. Bobin, V.A. Sadykov, V.A. Rogov, N.V. Mezentseva, G.M. Alikina, E.M. Sadovskaya, T.S. Glazneva, N.N. Sazonova, M.Y. Smirnova, S.A. Veniaminov, *Top. Catal.* 56 (2013) 958–968.
- [42] K. Nagaoka, Y. Abe, Y. Hashimoto, T. Ishikawa, K. Sato, Y. Takita, T. Wakatsuki, M. Kunisu, E. Suda, S. Inamoto, *ACS Catal.* 3 (2013) 1564–1572.
- [43] L. Mo, K.K.M. Leong, S. Kawi, *Catal. Sci. Technol.* 4 (2014) 2107–2114.
- [44] B. de Caprariis, P. de Filippis, V. Palma, A. Petrullo, A. Ricca, C. Ruocco, M. Scarsella, *Appl. Catal. A: Gen.* 517 (2016) 47–55.
- [45] N.H. Elsayed, N.R.M. Roberts, B. Joseph, J.N. Kuhn, *Appl. Catal. B: Environ.* 179 (2015) 213–219.
- [46] W.-J. Cai, L.-P. Qian, B. Yue, H.-Y. He, *Chin. Chem. Lett.* 25 (2014) 1411–1415.
- [47] A.T. Ashcroft, A.K. Cheetham, M.L.H. Green, P.D.F. Vernon, *Nature* 352 (1991) 225–226.
- [48] J. Wei, E. Iglesia, *J. Phys. Chem. B* 108 (2004) 7253–7262.
- [49] S. Saadi, F. Abild-Pedersen, S. Helveg, J. Sehested, B. Hinnemann, C.C. Appel, J.K. Nørskov, *J. Phys. Chem. C* 114 (2010) 11221–11227.
- [50] A. Álvarez, M.A. Centeno, J.A. Odriozola, *Top. Catal.* 59 (2016) 303–313.
- [51] J.H. Jeong, J.W. Lee, D.J. Seo, Y. Seo, W.L. Yoon, D.K. Lee, D.H. Kim, *Appl. Catal. A: Gen.* 302 (2006) 151–156.
- [52] C. Crisafulli, S. Scirè, S. Minicò, L. Solarino, *Appl. Catal. A: Gen.* 225 (2002) 1–9.
- [53] C. Crisafulli, S. Scirè, R. Maggiore, S. Minicò, S. Galvagno, *Catal. Lett.* 59 (1999) 21–26.
- [54] A.I. Tsyganok, M. Inaba, T. Tsunoda, K. Uchida, K. Suzuki, K. Takehira, T. Hayakawa, *Appl. Catal. A: Gen.* 292 (2005) 328–343.
- [55] D. Li, I. Atake, T. Shishido, Y. Oumi, T. Sano, K. Takehira, *J. Catal.* 250 (2007) 299–312.
- [56] F. Morales-Cano, L.F. Lundegaard, R.R. Tiruvalam, H. Falsig, M.S. Skjøth-Rasmussen, *Appl. Catal. A: Gen.* 498 (2015) 117–125.
- [57] K.K. Zhu, W. Hua, W. Deng, R.M. Richards, *Eur. J. Inorg. Chem.* (2012) 2869–2876.
- [58] B. Song, C. Wu, J. Chang, *Acta Biomater.* 8 (2012) 1901–1907.
- [59] G. Ertl, H. Knözinger, J. Weitkamp, *Handbook of Heterogeneous Catalysis*, 2nd ed., Wiley VCH Press, 2008 pp. 1380.
- [60] T. Osaki, T. Mori, *React. Kinet. Catal. Lett.* 89 (2006) 333–339.
- [61] T. Osaki, *Catal. Lett.* 145 (2015) 1931–1940.
- [62] H. Xiao, Z. Liu, X. Zhou, K. Zhu, *Catal. Commun.* 34 (2013) 11–15.
- [63] G.S. Hutchings, Y. Zhang, J. Li, B.T. Yonemoto, K.K. Zhu, F. Jiao, X.G. Zhou, *J. Am. Chem. Soc.* 137 (2015) 4223–4229.
- [64] M. Yu, K. Zhu, Z. Liu, H. Xiao, W. Deng, X. Zhou, *Appl. Catal. B: Environ.* 148–149 (2014) 177–190.
- [65] K.P. Gupta, *J. Phase Equilib. Diffus.* 25 (2004) 479–483.
- [66] D. Ugur, A.J. Storm, R. Verberk, J.C. Brouwer, W.G. Sloof, *J. Phys. Chem. C* 116 (2012) 26822–26828.
- [67] Y. Wang, H. Liu, B. Xu, J. Mol. Catal. A: Chem. 299 (2009) 44–52.
- [68] A. Pargaliana, F. Arena, F. Frusteri, N. Giordano, *J. Chem. Soc. Faraday Trans.* 86 (1990) 2663–2669.
- [69] J.G. Jakobsen, T.L. Jørgensen, I. Chorkendorff, J. Sehested, *Appl. Catal. A: Gen.* 377 (2010) 158–166.
- [70] D. Li, R. Li, M. Lu, X. Lin, Y. Zhan, L. Jiang, *Appl. Catal. B: Environ.* 200 (2017) 566–577.
- [71] D.C. Carvalho, H.S.A. de Souza, J.M. Filho, A.C. Oliveira, A. Campos, É.R.C. Milet, F.F. de Sousa, E. Padron-Hernandez, A.C. Oliveira, *Appl. Catal. A: Gen.* 473 (2014) 132–145.
- [72] I. Luisetto, C. Sarno, D. De Felici, F. Basoli, C. Battocchio, S. Tuti, S. Licocchia, E. Di Bartolomeo, *Fuel Process. Technol.* 158 (2017) 130–140.
- [73] W. Chen, G. Zhao, Q. Xue, L. Chen, Y. Lu, *Appl. Catal. B: Environ.* 136–137 (2013) 260–268.
- [74] M. Matsukata, T. Matsushita, K. Ueyama, *Energy Fuel* 9 (1995) 822–828.
- [75] J. Polanski, T. Siudya, P. Bartczak, M. Kapkowski, W. Ambroziewicz, A. Nobis, R. Sitko, J. Klimontko, J. Szade, J. Lelątko, *Appl. Catal. B: Environ.* 206 (2017) 16–23.
- [76] A.F. Carley, S.D. Jackson, J.N. O'Shea, M.W. Roberts, *Surf. Sci.* 440 (1999) 868–874.
- [77] L. Guzzi, G. Stefler, O. Gesztzi, I. Sajó, Z. Pászti, A. Tompos, Z. Schay, *Appl. Catal. A: Gen.* 375 (2010) 236–246.
- [78] A.F. Carley, S.D. Jackson, J.N. O'Shea, M.W. Roberts, *Phys. Chem. Chem. Phys.* 3 (2001) 274–281.
- [79] G. Nanse, E. Papirer, P. Fioux, F. Moguet, A. Tressaud, *Carbon* 35 (1997) 371–388.
- [80] J.P. Coutures, R. Erre, D. Massiot, C. Landron, D. Billard, G. Peraudeau, *Radiat. Effects* 98 (1986) 83–91.
- [81] H. Onishi, C. Egawa, T. Aruga, Y. Iwasawa, *Surf. Sci.* 191 (1987) 479–491.
- [82] Y.-A. Zhu, D. Chen, X.-G. Zhou, W.-K. Yuan, *Catal. Today* 148 (2009) 260–267.
- [83] C. Fan, Y.-A. Zhu, M.-L. Yang, Z.-J. Sui, X.-G. Zhou, D. Chen, *Ind. Eng. Chem. Res.* 54 (2015) 5901–5913.
- [84] B. AlSabbani, L. Falivene, S.M. Kozlov, A. Aguilar-Tapia, S. Ould-Chikh, J.-

- L. Hazemann, L. Cavallo, J.-M. Basset, K. Takanabe, *Appl. Catal. B: Environ.* 213 (2017) 177–189.
- [85] R.C. Egeberg, I. Chorkendorff, *Catal. Lett.* 77 (2001) 207–213.
- [86] A. Ruban, B. Hammer, P. Stoltze, H.L. Skriver, J.K. Nørskov, *J. Mol. Catal. A: Chem.* 115 (1997) 421–429.
- [87] J.B. Miller, H.R. Siddiqui, S.M. Gates, J.N. Russell, J.T. Yates, J.C. Tully, M.J. Cardillo, *J. Chem. Phys.* 87 (1987) 6725–6732.
- [88] K.V. Kumar, K. Porkodi, F. Rocha, *Catal. Commun.* 9 (2008) 82–84.
- [89] Y. Xu, A.C. Lausche, S. Wang, T.S. Khan, F. Abildpedersen, F. Studt, J.K. Nørskov, T. Bligaard, *New J. Phys.* 15 (2013) 5021–5038.
- [90] S.G. Wang, D.B. Cao, Y.W. Li, J. Wang, H. Jiao, *J. Phys. Chem. B* 110 (2006) 9976–9983.
- [91] S.G. Wang, X.Y. Liao, J. Hu, D.B. Cao, Y.W. Li, J. Wang, H. Jiao, *Surf. Sci.* 601 (2007) 1271–1284.
- [92] M.C.J. Bradford, M.A. Vannice, *Appl. Catal. A: Gen.* 142 (1996) 97–122.